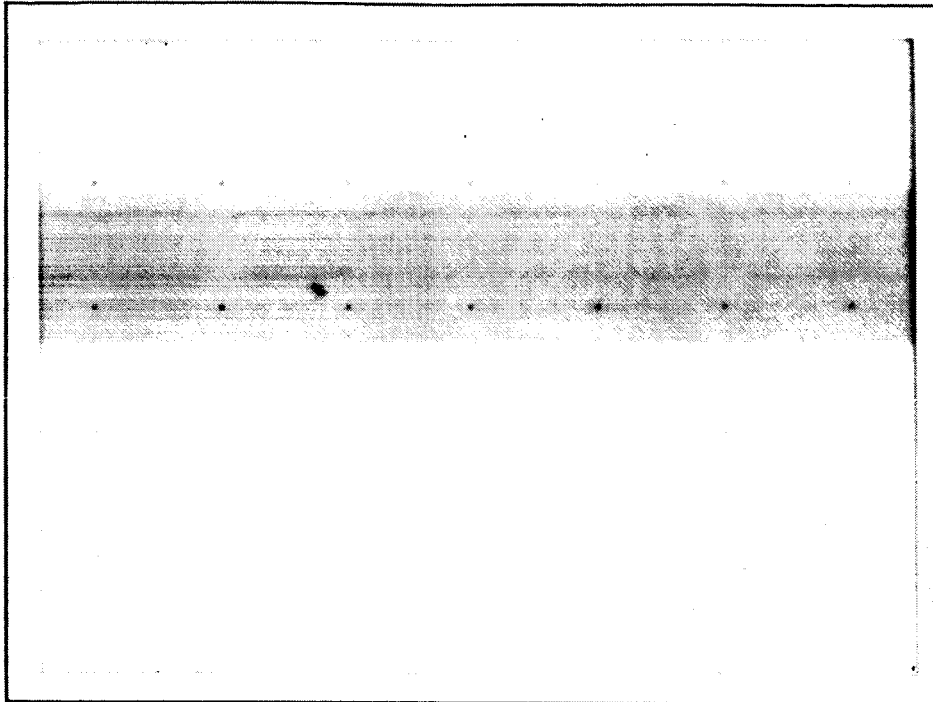


HA GRANT, IN-89-CR

87892

115P.

C S S A



**CENTER FOR SPACE SCIENCE AND ASTROPHYSICS**  
**STANFORD UNIVERSITY**  
**Stanford, California**

(NASA-CR-181196) NONLINEAR FORCE-FREE  
MAGNETIC FIELDS: CALCULATION AND APPLICATION  
TO ASTROPHYSICS Ph.D. Thesis (Stanford  
(Liv.) 115 p Avail: NTIS BC AC6/RF A01

N87-27567

Unclass

USC1 03A G3/89 0087892

NONLINEAR FORCE-FREE MAGNETIC FIELDS:  
CALCULATION AND APPLICATION TO ASTROPHYSICS

by  
Wei-Hong Yang

CSSA-ASTRO-87-11  
March 1987

A Dissertation  
Submitted to the Department of Applied Physics  
and the Committee on Graduate Studies  
of Stanford University  
in Partial Fulfillment of the Requirements  
for the Degree of  
Doctor of Philosophy

## ABSTRACT

The problem concerned in this work is that of calculating magnetic field configurations in which the Lorentz force  $\vec{j} \times \vec{B}$  is everywhere zero, subject to specified boundary conditions. We choose to represent the magnetic field in terms of Clebsch variables in the form  $\vec{B} = \nabla\alpha \times \nabla\beta$ . These variables are constant on any field line. The most appropriate choice of boundary conditions is to specify the values of  $\alpha$  and  $\beta$  on the bounding surface. We image that the field lines move in the direction of local Lorentz force and relax towards a force-free field configuration. This concept leads to an iteration procedure for modifying the variables  $\alpha$  and  $\beta$  that tends asymptotically towards the force-free state. We apply this method first to a simple problem in two rectangular dimensions; the calculation shows that the convergence of magnetic field energy to a minimum state(force-free) is close to exponential. We then apply this method to study some astrophysical force-free magnetic fields, such as the structures and evolution of magnetic fields of rotating sunspots and accretion disks. The implication of the results, as related to the mechanisms of solar flares, extragalactic radio sources and radio jets, are discussed.

**PRECEDING PAGE BLANK NOT FILMED**

## ACKNOWLEDGMENT

I wish to express my appreciation to my thesis advisor Prof. P.A. Sturrock, who suggested and supervised the work reported in this thesis. I have learned a lot from his lectures and many discussions. I also wish to thank scientists and my fellow graduate students of the Center for Space Sciences and Astrophysics for their warm friendship. I owe special thanks to Louise Meyers for her constant assistance along the whole period of my graduate study.

This work was supported in part by the Office of Naval Research Contract N00014-85-K-0111, NASA Grants NGL05-020-272 and NAGW-092, and NSF Grant ATM8414380.

## TABLE OF CONTENTS

Abstract .....	iii
Acknowledgement .....	iv
Table of Contents .....	v
List of Figures .....	vii
List of Tables .....	x
1. Introduction.....	1
2. Basic Physics of Force-Free Field .....	12
2.1. Magnetic Force.....	12
2.2. Clebsch Variables.....	16
2.3. Motion of Field Lines.....	22
2.4. Variational Principles.....	25
3. Numerical Formulation.....	28
3.1. Iteration Formulation.....	28
3.2. Finite Difference Method .....	32
3.3. Adjustable Grid Sizes.....	34
(a) Multigrid Method .....	35
(b) Adaptive-Grid Technique.....	36

(c) Spherical Coordinates .....	39
4. Test Model .....	41
5. Rotational Sunspot Model .....	55
5.1. Solar Flare and Magnetic Field .....	55
5.2. Modified Barnes-Sturrock Model .....	57
5.3. On the Influence of the Boundary .....	71
6. Accretion Disk Model .....	76
6.1. Keplerian Disk Model .....	76
6.2. Force-Free Field Models and Calculation .....	78
(a) Single Field Model .....	80
(b) Calculation of Magnetic Torque .....	82
(c) Multi-field Models .....	86
6.3. Extra-Galactic Radio Sources and the Accretion-Disk Flare Model. . .....	88
7. Discussion .....	97
7.1. On the Numerical Method .....	97
7.2. On the Astrophysical Application .....	99
References .....	103

## LIST OF FIGURES

Figure 1	Illustration of the boundary situation for evaluating the total magnetic force .....	14
Figure 2	A sketch of the intersection of $\alpha = \text{constant}$ , $\beta = \text{constant}$ defining a line of force of the magnetic field $\vec{B} = \nabla\alpha \times \nabla\beta$ .....	17
Figure 3	(a) The two magnetic flux-tubes $\Phi_1$ , $\Phi_2$ are linked in such a way as to give positive magnetic helicity. (b) A flux-tube $\Phi$ in the form of a right-handed trefoil knot .....	20
Figure 4	Illustration of panels with variational sizes .....	38
Figure 5	Vertical and horizontal sections through a force-free magnetic configuration described by equation (4.6) with $B_0 = 2.0$ , $k = 1.0$ , and $l = 0.8$ .....	44
Figure 6	Contours of constant- $\alpha$ (projection of field lines) and constant- $\gamma$ for two dimensional problem described in Chapter 4. Calculation was performed on a very coarse mesh ( $8 \times 8$ ).	
	(a) the assumed initial field configuration .....	47
	(b) field configuration after 5 iterations .....	48
	(c) field configuration after 15 iterations .....	49
	(d) field configuration after 60 iterations .....	50

Figure 7	The excess energy of the computed force-free field over the energy of the exact field, as a function of iteration number, for the case described in Chapter 4 .....	52
Figure 8	An example of spiral topology of filaments near a sunspot in $H_\alpha$ observation (Big Bear Observatory, 9 September 1970) and the configuration of lines of force of force-free magnetic fields; a1, a2 the $B^{(0)}$ -field (the simplest solution) and b1, b2 the $B^{(1)}$ -field (the next solution) for the spiral angle $45^\circ$ (Nakagawa et al., 1971) .....	58
Figure 9	Contours of constant $\alpha$ (projection of field lines on the $r - z$ plane) for the force-free field model of cylindrical symmetry described in chapter 5, with a sequence of twisting parameter $\gamma_M$ , the relative rotation of the regions of positive and negative polarity. Figure 9(h) gives the contour of constant $\alpha$ for the corresponding open-field configuration.	
(a)	$\gamma_M = 0$ , the potential field; (b) $\gamma_M = 0.5\pi$ .....	65
(c)	$\gamma_M = \pi$ ; (d) $\gamma_M = 1.5\pi$ .....	66
(e)	$\gamma_M = 2\pi$ ; (f) $\gamma_M = 2.5\pi$ .....	67
(g)	$\gamma_M = 3\pi$ ; (h) the corresponding open-field configuration .....	68
Figure 10	The magnetic field energy of the modified Barnes-Sturrock model of Chapter 5 as a function of $\gamma_M$ , which measures the relative rotation of the positive polarity region and the negative polarity region in a cylindrically symmetric system. Also shown is the energy of the corre-	



	sponding open-field configuration .....	70
Figure 11	A comparison of magnetic field configurations of the modified Barnes-Sturrock model calculated on meshes with different scale sizes. (a) Computation performed on $80 \times 80$ mesh. (b) Computation performed on $480 \times 480$ mesh with variable grid sizes. Shown in this figure is a section ( $320 \times 320$ ) of the result .....	75
Figure 12	Illustration of the differential rotation of a Keplerian accretion disk .....	79
Figure 13	Contours of constant $\alpha$ for a single force-free field model of a Keplerian accretion disk. The differential rotation angle between $R_1 = 16.0$ and $R_2 = 48.0$ is defined by $\gamma_M$ . (a) $\gamma_M = 0$ , potential field; (b) $\gamma_M = 2\pi$ .....	81
Figure 14	The magnetic field energy $W$ and magnetic torque $q$ of a single field model of a Keplerian accretion disk as functions of $\gamma_M$ .....	85
Figure 15	Contours of constant $\alpha$ for a double field model of an accretion disk. The differential rotation angle between $R_1 = 16.0$ and $R_2 = 80.0$ is defined by $\gamma_M$ . (a) $\gamma_M = 0$ ; (b) $\gamma_M = \pi$ ..... (c) $\gamma_M = 2\pi$ ; (d) $\gamma_M = 3\pi$ .....	89 90
Figure 16	Brightness distribution of the intense radio galaxy Cygnus A at 6 cm observed with the 6-second-of-arc beam of the Cambridge 1-mile aper-	

ture synthesis radio-telescope (taken from Mitton and Ryle, 1969) .	
.....	93

Figure 17 VLA maps of the jets in the radio galaxy M84 at 4.9 GHz, with the right panel showing detail of the central region. The peak on these maps is the radio core. Note the one-side bright base of the northern jet and the faint cocoon of emission flaring from both jets beyond 5" from the core (taken from Bridle and Perley, 1984) .....	94
--	----

## LIST OF TABLES

Table 1 Results of multigrid method on the test model of Chapter 4 .....	51
Table 2 Magnetic field energy as a function of rotation of the cylindrically symmetric model in Chapter 5 .....	69

## 1. INTRODUCTION

Magnetic fields play a key role in solar activities, and probably also in similar phenomena on other stars and in other astrophysical objects. Energetic bursts, such as solar flares, are widely believed to be a sudden release of energy stored in magnetic form in the solar atmosphere. One of the central problems in solar physics theory is to provide quantitative models of the transition of magnetic structures from slow passive evolution to fast active evolution leading to eruptive processes. Knowledge of the quiescent structure of the magnetic field is obviously an indispensable prerequisite for any study of the dynamics of these fields. For magnetohydrostatic equilibrium, the total force acting on the plasma, which in general includes the Lorentz force, the plasma-pressure gradient, and the gravitational force, must vanish everywhere. The equilibrium condition must be fulfilled, i.e.

$$-\nabla p + \vec{F}_m + \rho \vec{g} = 0, \quad (1.1)$$

where

$$\vec{F}_m \equiv \frac{1}{c} \vec{j} \times \vec{B} \quad (1.2)$$

is the Lorentz force;  $\rho$  and  $p$  are plasma density and pressure,  $\vec{g}$  is the gravitational field. If the magnetic field is strong enough, or say, any pressure gradient and gravitational force is dominated by the Lorentz force, the equilibrium configuration of the magnetic field is determined mainly by the magnetic force. The equilibrium requires that the Lorentz force  $\vec{F}_m$  must everywhere be zero. Mag-

netic fields satisfying this condition,

$$\vec{j} \times \vec{B} = 0, \quad (1.3)$$

or

$$(\nabla \times \vec{B}) \times \vec{B} = 0, \quad (1.4)$$

are called force-free. Generally force-free fields carry electrical currents, which align themselves along the magnetic field lines.

A particular case of a force-free field when  $\vec{j} = 0$  everywhere is called current-free. Together with the Maxwell equation  $\nabla \cdot \vec{B} = 0$ , a current-free magnetic field yields

$$\nabla^2 \vec{B} = 0, \quad (1.5)$$

or we may write

$$\vec{B} = \nabla \psi, \quad (1.6)$$

where  $\psi$  is the scalar magnetic potential, which satisfies Laplace's equation

$$\nabla^2 \psi = 0. \quad (1.7)$$

A current-free magnetic field is also called a potential field. If  $B_n (= \frac{\partial \psi}{\partial n})$  is prescribed on the boundary surface, the corresponding potential field contains the smallest possible amount of magnetic energy. Thus magnetic fields with non-zero currents but the same  $B_n$  on the boundary must contain more energy than the potential field. We will discuss the energy theorem in more detail in Chapter 2.

We now assume that the gravitational term  $\rho\vec{g}$  is negligible. According to equation (1.1), an equilibrium requires

$$\frac{1}{c} \vec{j} \times \vec{B} = \nabla p. \quad (1.8)$$

By substituting Ampere's law

$$\vec{j} = \frac{c}{4\pi} (\nabla \times \vec{B}), \quad (1.9)$$

equation (1.8) can be written as

$$\frac{1}{4\pi} (\nabla \times \vec{B}) \times \vec{B} = \nabla p. \quad (1.10)$$

Therefore, we obtain

$$\sin\vartheta = \frac{|\nabla p|}{\frac{1}{4\pi} |\nabla \times \vec{B}| |\vec{B}|}, \quad (1.11)$$

where  $\vartheta$  denotes the angle between the current and the magnetic field. Within an order of magnitude, the derivatives may be estimated approximately as

$$\nabla p \approx L^{-1} p, \quad (1.12)$$

$$|\nabla \times \vec{B}| \approx L^{-1} B, \quad (1.13)$$

where  $L$  is a characteristic dimension of the system concerned. With these approximations, we may derive a scaling relationship for equation (1.11), i.e.

$$\sin\vartheta \approx \frac{1}{2} \beta, \quad (1.14)$$

where  $\beta$  is the ratio of the plasma pressure to the magnetic pressure and is defined as

$$\beta \equiv \frac{p}{\frac{1}{8\pi} B^2}, \quad (1.15)$$

from which we know that  $\vartheta \approx 0$ , i.e.  $\vec{j}$  is nearly parallel to  $\vec{B}$ , if  $\beta \ll 1$ . This approximation indicates that the condition for a magnetic field configuration to be force-free is that the magnetic field energy density  $\frac{1}{8\pi}B^2$  is much larger than the gas pressure  $nkT$ .

The parameter  $\beta$  may be rewritten as

$$\beta \equiv \frac{nkT}{\frac{1}{8\pi}B^2} = 10^{-14.5} \frac{nT}{B^2}. \quad (1.16)$$

For the solar corona, electron number density  $n_e \sim 10^9 \text{ cm}^{-3}$ , temperature  $T \sim 10^6 \text{ K}^\circ$ , so we expect the field to be approximately force-free if  $B \gtrsim 10 \text{ Gauss}$ . Magnetic field is nearly in a force-free state for the high chromosphere of active regions where the magnetic field is strongly enhanced (Švestka, 1976). Magnetic fields may be taken to be force-free in the geomagnetosphere, and in many other astrophysical situations, for examples, the magnetospheres of active galactic nuclei with accretion discs (Blandford, 1976; Buckeley, 1981), and the extragalactic magnetized radio jets (Königl and Choudhuri, 1985).

The interest of studying the force-free magnetic field generally has two aspects. First, the equilibria of low-beta (  $\beta \ll 1$  ) cosmic plasma must be in force-free field configurations. As we know, the magnetohydrostatics is relevant to a variety of solar structures that appear to remain motionless for long periods of times. It has been applied, for example, to the overall structure of sunspots and of prominences, and to the large scale of coronal magnetic field, which often appears stationary for times long compared with the Alfvén travel time. The physical appearances of the cos-

mic plasma clouds, observed over a wide range of wavelengths, ranging from radio waves, visual light to x-ray, or  $\gamma$ -ray, combined with knowledge of the magnetic field structures, may give us useful information about the origins and the evolutions of the striking astrophysical objects, such as extragalactic radio sources, including radio jets. The another important aspect is that the force-free magnetic field is one of the most probable candidate configuration for energy conversion and storage. As is well-known, free magnetic field energy could be created by distorting a potential field slowly to force-free states. Most of the current solar flare models (Švestka, 1976; Sturrock, 1980) suggest that this kind of free magnetic field energy may be stored in the force-free coronal magnetic field due to the motion of the photosphere. If the instability sets in and a fast reconnection of the magnetic field occurs, this free field energy may be released eruptively and produce solar flares. Similar processes may also happen in other astrophysical objects, for example, the field evolution on a magnetized accretion disk.

Now we come to investigate theoretical solutions to the force-free field. The force-free field equation (1.3) can also be written as

$$\nabla \times \vec{B} = \lambda \vec{B}, \quad (1.17)$$

where  $\lambda$  is some scalar function of position, which represents the ratio of the electric current to the field strength. By taking the divergence of equation (1.17) after using  $\nabla \cdot \vec{B} = 0$ , the left-hand side vanishes, and the right-hand side reduces

to

$$(\vec{B} \cdot \nabla)\lambda = 0, \quad (1.18)$$

which means that the quantity  $\lambda$  must be constant along each line of force.

Let us assume that  $\vec{B}_1, \vec{B}_2$  are solutions of equation (1.17), so that we may have

$$\begin{aligned} \nabla \times \vec{B}_1 &= \lambda_1(\vec{r}) \vec{B}_1, \\ \nabla \times \vec{B}_2 &= \lambda_2(\vec{r}) \vec{B}_2. \end{aligned} \quad (1.19)$$

By substituting the sum of  $\vec{B}_1$  and  $\vec{B}_2$  into the left side of equation (1.4), we obtain

$$[\nabla \times (\vec{B}_1 + \vec{B}_2)] \times (\vec{B}_1 + \vec{B}_2) = (\lambda_1 - \lambda_2)(\vec{B}_1 \times \vec{B}_2), \quad (1.20)$$

which vanishes when  $\lambda_1 = \lambda_2$  everywhere.

It is clear that the general problem represented by equation (1.3) or (1.17) is nonlinear. The sum of two separate solutions of those equations does not, in general, produce a third solution. However, if  $\lambda$  takes the same value on every field line ( i.e.,  $\lambda = \text{constant}$  everywhere), the curl of equation (1.17) reduces to

$$(\nabla^2 + \lambda^2)\vec{B} = 0, \quad (1.21)$$

where we used the relation  $\nabla \times (\nabla \times \vec{B}) = \nabla(\nabla \cdot \vec{B}) - \nabla^2 \vec{B} = -\nabla^2 \vec{B}$ . Equation (1.21) is the well-known Helmholtz equation, which can be solved by standard methods. Obviously, we now have a linear equation form, while this category of force-free field is called the 'constant- $\lambda$ ' or 'constant- $\alpha$ ' (some-



times the parameter is denoted by  $\alpha$ ) force-free field, or linear force-free field.

The basic force-free equation (1.3) or (1.17) has a disarmingly simple form, but it is difficult to find general solutions because of their nonlinearity. So, much effort has been made to solve the linear equation (1.18), and the solutions have been obtained in various configurations. For example, by considering solutions to equation (1.21) which are required to satisfy  $\nabla \cdot \vec{B} = 0$ , we may write these solutions in the form

$$\vec{B} = \alpha \nabla \times (\psi \vec{a}) + \nabla \times (\nabla \times (\psi \vec{a})), \quad (1.22)$$

where  $\vec{a}$  is a fixed unit vector, and the scalar function satisfies

$$(\nabla^2 + \alpha^2)\psi = 0. \quad (1.23)$$

Chandrasekhar and Kendall (1957) obtained the general solution of equation (1.23) with  $\vec{a} = \hat{r}$  in spherical coordinates  $(r, \theta, \phi)$

$$\psi = \sum_{n=0}^{\infty} \sum_{m=0}^{\infty} A_n^m r^{-1/2} J_{n+\frac{1}{2}}(\alpha r) P_n^m(\cos\theta) e^{im\phi}, \quad (1.24)$$

in terms of Bessel functions ( $J_n$ ) and associated Legendre functions ( $P_n^m(\cos\theta)$ ), which leads to force-free magnetic field solutions by substituting it into equation (1.22). About other solutions to equation (1.23) one may refer to the works in rectangular coordinates by Nakagawa and Raadu (1972), and in cylindrical coordinates by Priest (1982). An alternative prescription to equation (1.22) for axisymmetric solutions was obtained by Lüst and Schlüter (1954).

However, the intensive studies concerning the comparison between the observation of solar magnetic field structure and the calculation performed on the constant- $\lambda$  model show that the assumed constancy of  $\lambda$  is poorly satisfied (Levine 1976). In many cases it can be found that the variation of the electric current  $\vec{j}$  with respect to  $\vec{r}$  is clearly incompatible with the assumption that  $\lambda$  is constant. For example, suppose that we are trying to find the force-free field configuration produced by a finite source such as a pair of sunspots of opposite polarity. If we investigate the field at a large distance from the source, we expect that the field strength has the form  $B = B_0 r^{-n}$ . We find that this field will not be a linear force-free field, because in this case

$$\lambda = \frac{|\nabla \times \vec{B}|}{|\vec{B}|} \propto \frac{1}{r}, \quad (1.25)$$

which obviously contradicts the requirement that  $\lambda = \text{constant}$ . Hence the assumption that  $\lambda = \text{constant}$ , which reduces the nonlinear problem of (1.3) or (1.17) to the linear problem described by (1.21), is inappropriate for the investigation of a wide range of interesting problems of solar physics and astrophysics.

In the special case that the magnetic field configuration is independent of one of the spatial coordinates, it is possible to generate solutions of the nonlinear equation (1.4) by a special technique described by Priest (1982). For instance, consider a field configuration independent of  $y$  in rectangular cartesian coordinates. The components of the field may be specified by the

form

$$B_x = \frac{\partial A}{\partial z}, \quad B_y, \quad B_z = -\frac{\partial A}{\partial x}, \quad (1.26)$$

which satisfies  $\nabla \cdot \vec{B} = 0$  automatically. The components of equation (1.4) become

$$\begin{aligned} \nabla^2 A \frac{\partial A}{\partial x} + \frac{\partial}{\partial x} \left( \frac{1}{2} B_y^2 \right) &= 0, \\ \frac{\partial B_y}{\partial z} \frac{\partial A}{\partial x} - \frac{\partial B_y}{\partial x} \frac{\partial A}{\partial z} &= 0, \\ \nabla^2 A \frac{\partial A}{\partial z} + \frac{\partial}{\partial z} \left( \frac{1}{2} B_y^2 \right) &= 0. \end{aligned} \quad (1.27)$$

We find that  $B_y$  is a function of the flux function ( $A$ ) alone and so it remains constant along a field line in the surface  $A = \text{constant}$ . If we write

$$B_y = F(A), \quad (1.28)$$

we obtain from equation (1.27)

$$\frac{\partial^2 A}{\partial x^2} + \frac{\partial^2 A}{\partial z^2} + \frac{d}{dA} \left( \frac{1}{2} F^2(A) \right) = 0, \quad (1.29)$$

which is in general a nonlinear equation. For each specified function  $F(A)$ , this is a technique for generating a special set of solutions of the nonlinear equation. The particular cases  $B_y = \text{constant}$  and  $B_y = \text{constant} \times A$  give potential and constant- $\lambda$  fields, respectively. However, this procedure is inappropriate for solving the general problem, such as computing the force-free field that satisfies specified boundary conditions.

The investigation of the general ( $\lambda = \lambda(\vec{r})$ ) force-free magnetic field has already been made in the two-dimensional case by Sturrock and Woodbury (1967),

and Barnes and Sturrock (1972) in the context of simulating the coronal magnetic field evolution and the flare-energy build-up; and further by Sakurai (1979). We will discuss their works in a special section 2.2, since all their works involved describing magnetic field in terms of the Clebsch variables. In another article, Sakurai (1981) has discussed another method for solving the force-free equation (1.17) with spatially varying  $\lambda$ . If the distribution of the normal component of the magnetic field  $B_n$  is given on a bounding surface, and if  $\lambda$  is specified as well either in the region of the surface where  $B_n$  is positive or in the region where  $B_n$  is negative, the magnetic field can be found by an iterative process. Starting from the potential field with the given  $B_n$ , the value of  $\lambda$  is used to distribute currents along the field lines. The field is then recalculated, and the procedure repeated until the calculation converges. This method has an advantage, comparing to his previous work (Sakurai, 1979), that one can specify not only the position of the endpoints but also the position of any intermediate point on a field line.

The aim of this work is to develop a new practical and efficient method of computing the general force-free field, and then apply the method to problems of interest in solar physics and astrophysics. The basic physics of force-free magnetic fields related to our work will be described briefly in Chapter 2. In Chapter 3, we will discuss the basic idea leading to the formulation of a new numerical scheme of computing force-free field, and describe the computational knowledge needed for the practical use of the method. A

test case of the method will be shown in Chapter 4. The applications to a rotational sunspot model and to accretion disk models will be discussed in Chapter 5 and Chapter 6, respectively. We discuss the future development of the method and further application to physics problems in the final chapter.

## 2. BASIC PHYSICS OF FORCE-FREE FIELD

### 2.1. Magnetic Force

By using the vector identity

$$\nabla(\vec{a} \cdot \vec{b}) = (\vec{a} \cdot \nabla)\vec{b} + (\vec{b} \cdot \nabla)\vec{a} + \vec{a} \times (\nabla \times \vec{b}) + \vec{b} \times (\nabla \times \vec{a}), \quad (2.1)$$

we may rewrite equation (1.2) into the form

$$\vec{F}_m = \frac{1}{4\pi}(\vec{B} \cdot \nabla)\vec{B} - \nabla\left(\frac{B^2}{8\pi}\right). \quad (2.2)$$

This equation shows that the magnetic force is equivalent to a magnetic hydrostatic pressure,

$$p_m = \frac{B^2}{8\pi} \quad (2.3)$$

plus a term which can be thought of as a tension along the lines of force. For a force-free configuration, these two terms must cancel everywhere. For some simple geometrical situations, such as the magnetic field  $\vec{B}$  having only one component, the additional tension term vanishes. If the plasma system is in an equilibrium state, the magnetic hydrostatic pressure  $p_m$  must be balanced by some other pressure, therefore the field configuration will not be the force-free case.

Equation (2.2) can be expressed in tensor form as

$$F_i = \frac{\partial}{\partial x_k} \left( \frac{B_i B_k}{4\pi} \right) - \frac{\partial}{\partial x_k} \left( \frac{B^2}{8\pi} \delta_{ik} \right). \quad (2.4)$$

With the definition of the Maxwell stress tensor  $T_{ik}$  (Jackson, 1962) as

$$T_{ik} = \frac{1}{4\pi}[E_i E_k + B_i B_k - \frac{1}{2}(\vec{E} \cdot \vec{E} + \vec{B} \cdot \vec{B})\delta_{ik}], \quad (2.5)$$

equation (2.4) can be rewritten in component form as

$$F_i = \frac{\partial T_{ik}}{\partial x_k}, \quad (2.6)$$

so that the magnetic force is the divergence of the Maxwell tensor  $\mathbf{T}$  when the electric field terms are neglected. The force-free field configuration means

$$\nabla \cdot \mathbf{T} = 0, \quad (2.7)$$

everywhere.

We consider an arbitrary volume  $V$ . The total force acting on  $V$  can be calculated by the integral (Alfvén and Fälthammar, 1963)

$$\vec{F}_{tot} = \int_V \vec{F}_m dV. \quad (2.8)$$

By using the vector identities

$$\int_V \nabla \phi dV = \int_S \phi d\vec{S} \quad (2.9)$$

and

$$\int_V (\vec{a} \cdot \nabla) \vec{b} dV = \int_S \vec{b} (\vec{a} \cdot d\vec{S}) - \int_V \vec{b} \nabla \cdot \vec{a} dV, \quad (2.10)$$

we obtain

$$\vec{F}_{tot} = \int_S \left(-\frac{B^2}{8\pi}\right) d\vec{S} + \int_S \frac{\vec{B}(\vec{B} \cdot d\vec{S})}{4\pi}, \quad (2.11)$$

where  $S$  is the surface of the volume  $V$ . If we write  $d\vec{S} = \hat{n}dS$ ,  $\vec{B} = B\hat{b}$ , where  $\hat{n}$  and  $\hat{b}$  are the unit vectors of  $\vec{S}$  and  $\vec{B}$ , respectively (see Figure 1). We know that

$$\vec{B} \cdot d\vec{S} = B(\hat{b} \cdot \hat{n})dS = B \cos\theta dS, \quad (2.12)$$

where  $\theta$  is the angle between the magnetic field and the surface normal vector.

So we can write the equation (2.11) as

$$\vec{F}_{tot} = - \int_S \frac{B^2}{8\pi} \hat{n} dS + \int_S \frac{B^2}{4\pi} \hat{b} \cos\theta dS. \quad (2.13)$$

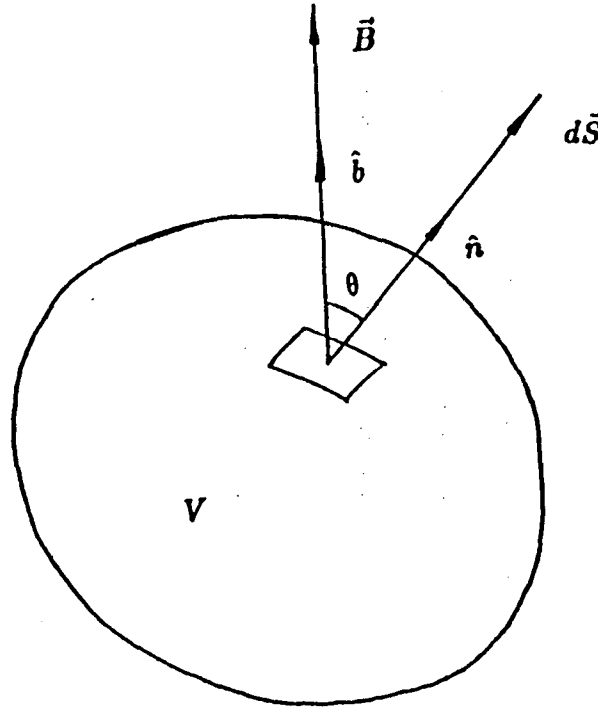


Figure 1. Illustration of the boundary situation for evaluating the total magnetic force.



The first term on the right-hand side of equation (2.13) represents a pressure of magnitude of  $\frac{B^2}{8\pi}$  and the second term represents a tension of magnitude  $\frac{B^2}{4\pi}$  directed along the lines of force. If  $\hat{b} \perp \hat{n}$  all over the boundary surface, then the second tension term vanishes, only the magnetic pressure on the boundary contributes to the total magnetic force  $\vec{F}_{tot}$ .

We now consider another volume integral (Chandrasekhar, 1961)

$$\int_V \vec{r} \cdot [(\nabla \times \vec{B}) \times \vec{B}] dV = \int_V (\nabla \times \vec{B}) \cdot (\vec{B} \times \vec{r}) dV. \quad (2.14)$$

With the aid of the identity

$$\int_V \vec{a} \cdot (\nabla \times \vec{b}) dV = \int_V \vec{b} \cdot (\nabla \times \vec{a}) dV - \int_S (\vec{a} \times \vec{b}) \cdot d\vec{S}, \quad (2.15)$$

the integral (2.14) can be rewritten as

$$\begin{aligned} \int_V \vec{r} \cdot [(\nabla \times \vec{B}) \times \vec{B}] dV &= \int_V \vec{B} \cdot \nabla \times (\vec{B} \times \vec{r}) dV - \int_S (\vec{B} \times \vec{r}) \times \vec{B} \cdot d\vec{S} \\ &= \frac{1}{2} \int_V B^2 dV - \frac{1}{2} \int_S B^2 \vec{r} \cdot d\vec{S} + \int_S (\vec{B} \cdot \vec{r}) \vec{B} \cdot d\vec{S}. \end{aligned} \quad (2.16)$$

Consequently, if the force-free condition is satisfied, i.e.  $(\nabla \times \vec{B}) \times \vec{B} = 0$ , inside  $V$ , we have

$$\int_V B^2 dV = \int_S B^2 \vec{r} \cdot d\vec{S} - 2 \int_S (\vec{B} \cdot \vec{r}) \vec{B} \cdot d\vec{S}. \quad (2.17)$$

The value of the left-hand side of this equation is always positive. To satisfy this condition, the magnetic field strength on the boundary surface  $S$  can not all vanish. This indicates a constraint that an unconfined force-free field with no

boundary does not exist. All force-free fields must be confined by rigid boundaries or be anchored by magnetic field lines threading a boundary, the latter being the cases we are going to study in Chapter 5 (rotational sunspot model), and in Chapter 6 (accretion disk model), respectively.

## 2.2. Clebsch Variables

The magnetic field is solenoidal, i.e.  $\nabla \cdot \vec{B} = 0$ , and therefore can be represented by two scalars. One appropriate way of representing magnetic field is to introduce the Clebsch variables usually denoted by  $\alpha$  and  $\beta$ , with the property

$$\vec{B} = \nabla\alpha \times \nabla\beta. \quad (2.18)$$

We see that

$$\vec{B} \cdot \nabla\alpha = \vec{B} \cdot \nabla\beta = 0, \quad (2.19)$$

so  $\alpha$  and  $\beta$  are constant along the field line. By this definition  $\vec{B}$  is tangent to each of the families of surfaces  $\alpha = \text{constant}$  and  $\beta = \text{constant}$ . The line of intersection of any two such surfaces therefore defines a line of force characterized by the associated pair of Clebsch variables  $(\alpha, \beta)$ , as sketched in Figure 2.

The Clebsch variables are not uniquely defined, however. Any independent pair of solutions to (2.19) leads to some choice of  $\alpha$  and  $\beta$ . Given a pair of such potentials, an alternate choice is  $\eta(\alpha, \beta)$  and  $\xi(\alpha, \beta)$ , if

$$\frac{\partial(\eta, \xi)}{\partial(\alpha, \beta)} = 1, \quad (2.20)$$

is satisfied.

When the magnetic field is expressed in form of Clebsch variables, solving the force-free field equation becomes a task of seeking for two scalar functions  $\alpha$ ,  $\beta$  which represent the field and satisfy the force-free condition. Any change of the magnetic field will reflect on the corresponding variation of the families of  $\alpha = \text{constant}$  and  $\beta = \text{constant}$  surfaces.

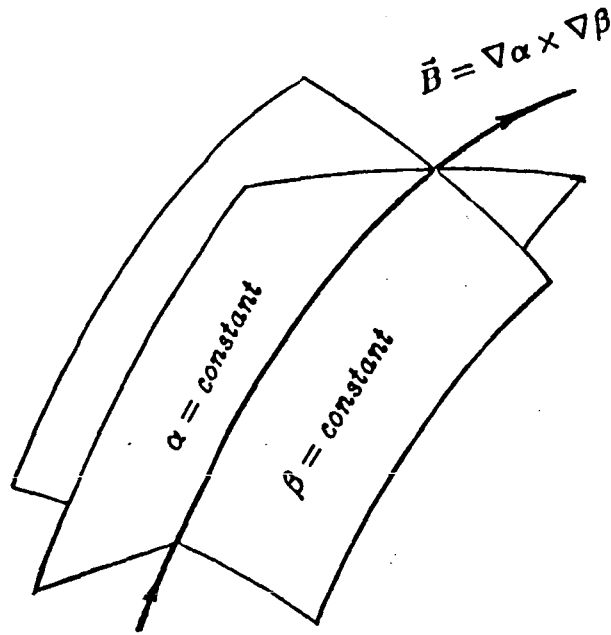


Figure 2. A sketch of the intersection of  $\alpha = \text{constant}$ ,  $\beta = \text{constant}$  defining a line of force of the magnetic field  $\vec{B} = \nabla\alpha \times \nabla\beta$ .

In many cases, the adoption of the Clebsch variables is convenient for numerical handling of the differential equations. Because of this advantage, the Clebsch variables were used in the pioneer works in solving a general force-free equation by Sturrock and Woodbury (1967), Barnes and Sturrock (1972), and in a later work by Sakurai (1979).

In terms of the description (2.18), equation (1.4), which specifies the force-free state, becomes

$$(\nabla \times \vec{B}) \times (\nabla \alpha \times \nabla \beta) = [(\nabla \times \vec{B}) \cdot \nabla \beta] \nabla \alpha - [(\nabla \times \vec{B}) \cdot \nabla \alpha] \nabla \beta = 0. \quad (2.21)$$

Thus we obtain

$$(\nabla \times \vec{B}) \cdot \nabla \alpha = 0, \quad (\nabla \times \vec{B}) \cdot \nabla \beta = 0, \quad (2.22)$$

or in term of the electric current

$$\vec{j} \cdot \nabla \alpha = 0, \quad \vec{j} \cdot \nabla \beta = 0. \quad (2.23)$$

Equations (2.18) can be written as

$$\begin{aligned} [\nabla \times (\nabla \alpha \times \nabla \beta)] \cdot \nabla \alpha &= 0, \\ [\nabla \times (\nabla \alpha \times \nabla \beta)] \cdot \nabla \beta &= 0, \end{aligned} \quad (2.24)$$

which can be further expressed in terms of dyadic notation as follows

$$\begin{aligned} (\nabla \beta)^2 \nabla^2 \alpha - \nabla \beta \nabla \beta : \nabla \nabla \alpha - (\nabla \alpha \cdot \nabla \beta) \nabla^2 \beta + \nabla \alpha \nabla \beta : \nabla \nabla \beta &= 0, \\ -(\nabla \alpha \cdot \nabla \beta) \nabla^2 \alpha + \nabla \alpha \nabla \beta : \nabla \nabla \alpha + (\nabla \alpha)^2 \nabla^2 \beta - \nabla \alpha \nabla \alpha : \nabla \nabla \beta &= 0. \end{aligned} \quad (2.25)$$

The force-free field equations are nonlinear in terms of the Clebsch variables; however, equations (2.25) are linear in the second derivatives.

Sturrock and Woodbury (1967) applied a relaxation method to solve these equations (2.25) for a problem in rectangular Cartesian coordinates. In their method, the values of Clebsch variables were adjusted at each mesh point to make - or tend to make - the field locally force-free. A similar method was applied to a problem in cylindrical coordinates by Barnes and Sturrock (1972).

Sakurai (1979) also describes the field in terms of Clebsch variables in a different approach to compute three-dimensional force-free magnetic field configurations. Based on the variational principles of the current-free and force-free magnetic fields, he employs the Rayleigh-Ritz method (Courant and Hilbert, 1953) of representing the field in terms of a set of base functions and solving for the coefficients arising in this representation.

Our recent work on computing the force-free field (Sturrock and Yang 1985; Yang, Sturrock and Antiochos, 1986), which we will discuss in the following chapters, also involves the Clebsch variables.

What is the applicable range of the Clebsch variables to represent a magnetic field configuration ? This question naturally arises for answer.

The expression (2.18) requires that  $\nabla\alpha$  and  $\nabla\beta$  must be continuous vector functions, so that the scalar functions  $\alpha(\vec{r})$  and  $\beta(\vec{r})$  must have no singularity. Obviously, for a possible expression of magnetic field in terms of Clebsch variables, no connection between any two surfaces of  $\alpha = \text{constant}$ , or any two surfaces of  $\beta = \text{constant}$  is allowed. As we shall show, it is impossible to construct field lines by the pairs of  $\alpha$  and  $\beta$ , if the field lines are linked or knotted

as shown in Figure 3. What can be represented by Clebsch variables are simple field configurations.

Concerning the complexity of the magnetic field configuration, one may recall the concept of magnetic helicity (Moffatt, 1983), which is defined as

$$H = \int_V \vec{B} \cdot \vec{A} d^3x \quad (2.26)$$

where  $\vec{A}$  is the vector potential.

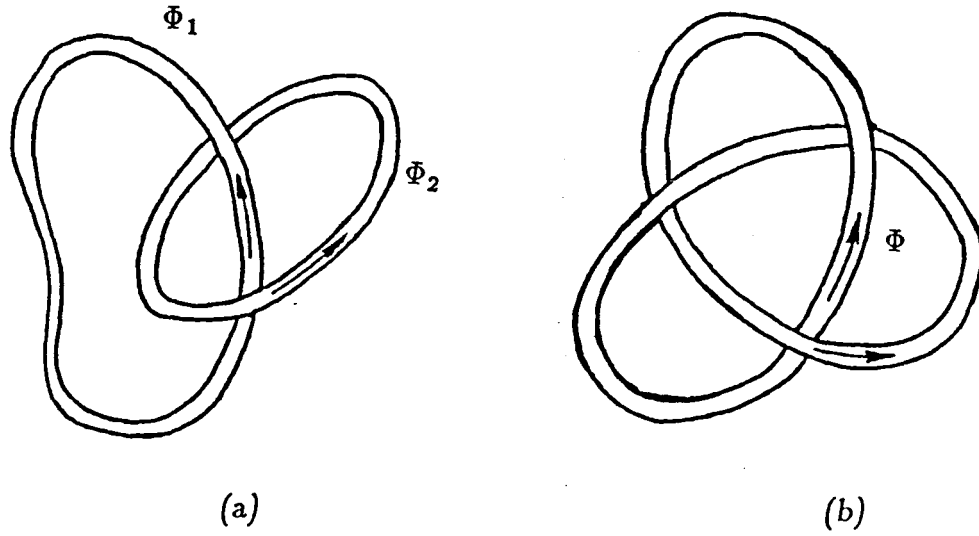


Figure 3. (a) The two magnetic flux-tubes  $\Phi_1$ ,  $\Phi_2$  are linked in such a way as to give positive magnetic helicity. (b) A flux-tube  $\Phi$  in the form of a right-handed trefoil knot.

The magnetic helicity is a measure of the degree of structural complexity of the  $\vec{B}$ -field, related to the 'interconnection' of the field. For two untwisted closed flux tubes linked once and with a volume of integration containing both tubes (Figure 3 (a)), we find that

$$H = \pm 2\Phi_1\Phi_2, \quad (2.27)$$

where  $\Phi_1$  and  $\Phi_2$  measure the magnetic flux of the tubes, and the sign of  $H$  depends on the relative orientation of linkage.

It may of course happen that  $\vec{A} \cdot \vec{B} \equiv 0$ ; this is the necessary and sufficient condition for the existence of Clebsch variables  $\alpha(\vec{r})$  and  $\beta(\vec{r})$  such that

$$\vec{A} = \alpha \nabla \beta, \quad \vec{B} = \nabla \alpha \times \nabla \beta, \quad (2.28)$$

which leads to

$$H \equiv 0. \quad (2.29)$$

In this situation, the magnetic field lines are the intersections of the surfaces  $\alpha = \text{constant}$ ,  $\beta = \text{constant}$ , and the  $\vec{A}$  - lines are everywhere orthogonal to the surface  $\alpha = \text{constant}$ . It is clear from the above discussion that magnetic fields having linked or knotted field lines can not admit such representation.

An associated problem is that of gauge-invariance : let  $\vec{A} \rightarrow \vec{A} + \nabla \chi$ . We may define an extended set of Clebsch variables  $\alpha, \beta, \chi$  by the equation

$$\vec{A} = \alpha \nabla \beta + \nabla \chi, \quad (2.30)$$

so that

$$\vec{B} \equiv \nabla \times \vec{A} = \nabla \alpha \times \nabla \beta. \quad (2.31)$$

We see that

$$\vec{A} \cdot \vec{B} = \nabla \chi \cdot (\nabla \alpha \times \nabla \beta). \quad (2.32)$$

Then from equation (2.26) the change in  $H$  is

$$\begin{aligned} \Delta H &= \int_V \nabla \chi \cdot (\nabla \alpha \times \nabla \beta) dV \\ &= \int_V \nabla \cdot (\chi \nabla \alpha \times \nabla \beta) dV \\ &= \int_S \chi \vec{B} \cdot \hat{n} dS \\ &= \int_S \chi B_n dS, \end{aligned} \quad (2.33)$$

Only if  $S$  is a magnetic surface, i.e.  $\hat{n} \cdot \vec{B} = 0$  on  $S$ , will the helicity integral be gauge-invariant ( $\Delta H = 0$ ). Conversely, if  $\Delta H \neq 0$  (as will happen if the magnetic field lines are knotted or linked), then equation (2.30) is not a possible global representation for  $\vec{A}$  and  $\vec{B}$ . Note that, if  $\hat{n} \cdot \vec{B}|_S \neq 0$ , we cannot simply choose to work in the Coulomb gauge in order to define  $H$ ; the Coulomb gauge is ill-defined inside  $V$  without a knowledge of the outside field (Berger and Field, 1984).

### 2.3. Motion of Field Lines

In classical fluid dynamics, the rate of change in some quantity  $\zeta$ , as observed by a particle moving with the fluid's velocity  $\vec{v}$ , is its 'material derivative' defined as

$$\frac{d\zeta}{dt} = \frac{\partial \zeta}{\partial t} + \vec{v} \cdot \nabla \zeta, \quad (2.34)$$



which vanishes if  $\zeta$  is convected with the flow. It therefore seems reasonable to find a similar way to demonstrate the motion of the field lines for a given magnetic field which changes with time. Obviously, one possibility is to use the Clebsch variables, which label the field lines.

One of the basic MHD equations (Boyd and Sanderson, 1969), the induction equation, is

$$\frac{\partial \vec{B}}{\partial t} = \nabla \times (\vec{v} \times \vec{B}) + \eta \nabla^2 \vec{B}, \quad (2.35)$$

where

$$\eta \equiv \frac{c^2}{4\pi\sigma}, \quad (3.36)$$

is the magnetic diffusivity. Here it is assumed that the electrical conductivity  $\sigma$  is constant in space.

For a fluid at rest ( $\vec{v} = 0$ ), equation (2.35) reduced to the diffusion equation

$$\frac{\partial \vec{B}}{\partial t} = \frac{c^2}{4\pi\sigma} \nabla^2 \vec{B}. \quad (2.37)$$

This means that an initial configuration of magnetic field will decay away in a 'diffusion time'

$$\tau \sim \frac{L^2}{\eta} = \frac{4\pi\sigma L^2}{c^2}, \quad (2.38)$$

where  $L$  is a length characteristic of the spatial variation of  $\vec{B}$ . For examples, for a typical sunspot magnetic field,  $L \sim 10^9 \text{ cm}$ ,  $\tau \sim 10^{14} \text{ s}$  ( $10^{6.5} \text{ years}$ ); for coronal fields, if  $L \sim 10^{10} \text{ cm}$ , therefore,  $\tau \sim 10^{16} \text{ s}$  ( $10^{9.5} \text{ years}$ ).

For a completely conductive plasma, the electrical conductivity  $\sigma \rightarrow \infty$ . More generally, for times short compared to the diffusion time  $\tau$ , the diffusion

term, i.e. the second term in the right-hand side of equation (2.35) is negligible.

We may then write

$$\frac{\partial \vec{B}}{\partial t} = \nabla \times (\vec{v} \times \vec{B}), \quad (2.39)$$

where  $\nabla \times (\vec{v} \times \vec{B})$  is the convection term. This indicates the so-called 'frozen-in' concept, that field lines are frozen into the fluid and are carried along bodily with it (Stern, 1966).

If we represent the  $\vec{B}$ -field in the Clebsch variables,  $\alpha$  and  $\beta$ , equation (2.39) becomes

$$\frac{\partial}{\partial t}(\nabla \alpha \times \nabla \beta) = \nabla \times [\vec{v} \times (\nabla \alpha \times \nabla \beta)], \quad (2.40)$$

which can be further written as

$$\begin{aligned} \nabla \alpha \times \nabla \frac{\partial \beta}{\partial t} - \nabla \beta \times \nabla \frac{\partial \alpha}{\partial t} &= \nabla \times [\vec{v} \times (\nabla \alpha \times \nabla \beta)] \\ &= \nabla \times [\nabla \alpha (\vec{v} \cdot \nabla \beta) - \nabla \beta (\vec{v} \cdot \nabla \alpha)] \\ &= \nabla (\vec{v} \cdot \nabla \beta) \times \nabla \alpha - \nabla (\vec{v} \cdot \nabla \alpha) \times \nabla \beta. \end{aligned}$$

Hence we have

$$\nabla \alpha \times \nabla \frac{d\beta}{dt} - \nabla \beta \times \nabla \frac{d\alpha}{dt} = 0, \quad (2.41)$$

where

$$\begin{aligned} \frac{d\alpha}{dt} &\equiv \frac{\partial \alpha}{\partial t} + \vec{v} \cdot \nabla \alpha, \\ \frac{d\beta}{dt} &\equiv \frac{\partial \beta}{\partial t} + \vec{v} \cdot \nabla \beta. \end{aligned} \quad (2.42)$$

There is a whole family of solutions to equation (2.41), but the simplest is

$$\frac{d\alpha}{dt} = \frac{d\beta}{dt} = 0. \quad (2.43)$$

That means, we are permitted to suppose that the Clebsch variables, and the intersection of the  $\alpha = \text{constant}$  and  $\beta = \text{constant}$  surfaces, that is the line of force, move with the fluid.

If we write the left-hand side of equation (2.40) as

$$\frac{\partial}{\partial t}(\nabla\alpha \times \nabla\beta) = \nabla \times \left( \frac{\partial\alpha}{\partial t} \nabla\beta - \frac{\partial\beta}{\partial t} \nabla\alpha \right), \quad (2.44)$$

we may obtain

$$\frac{\partial\alpha}{\partial t} \nabla\beta - \frac{\partial\beta}{\partial t} \nabla\alpha = \vec{v} \times \vec{B}, \quad (2.45)$$

which is satisfied by

$$\vec{v} = \left( \frac{\partial\beta}{\partial t} \nabla\alpha - \frac{\partial\alpha}{\partial t} \nabla\beta \right) \times \frac{\vec{B}}{B^2}. \quad (2.46)$$

This solution is not unique. Any velocity parallel to  $\vec{B}$  may be added to it without changing the validity of equation (2.43). In what follows, we set the parallel velocity to zero, so when discussing the velocity of a line of force, only the component perpendicular to  $\vec{B}$  is implied.

#### 2.4. Variational Principles for Force-Free Magnetic Field

As is well-known in basic electromagnetic theory, the current-free magnetic field is the state of stationary (usually minimum) energy subject to certain boundary condition. This can be expressed as the variational problem :

$$\delta W = \delta \int_V \frac{B^2}{8\pi} d^3x = 0, \quad (2.47)$$

where  $B_n$  is given on  $S$ .

This leads to  $\nabla \times \vec{B} = 0$ . It can be shown that the solution is unique and that it makes  $W$ , the total magnetic field energy inside the volume  $V$ , a minimum.

The situation is different if the volume  $V$  contains a plasma and the frozen-in condition of field lines is satisfied. For this case, an instantaneous value of  $B_n$  is not sufficient to determine the field configuration (Sturrock and Woodbury, 1967).

We consider a magnetic field that can be described by Clebsch variables  $\alpha(\vec{r})$  and  $\beta(\vec{r})$ , which are transported with the fluid as indicated in section 2.3. We now consider the variational problem :

$$\delta W \equiv \delta \int_V \frac{B^2}{8\pi} d^3x = 0, \quad (2.48)$$

where  $\alpha, \beta$  are given on  $S$ .

Note that now not only  $B_n$  is given on the boundary surface  $S$  but also the connection of field lines on  $S$  is given, because values of  $\alpha$  and  $\beta$  on  $S$  are fixed. This boundary condition leads in general to a magnetic field configuration carrying non-zero electric current. We find that

$$\begin{aligned} \delta W &\equiv \delta \left[ \frac{1}{8\pi} \int_V (\nabla \alpha \times \nabla \beta)^2 d^3x \right] \\ &= \frac{1}{4\pi} \int_V \vec{B} \cdot (\nabla(\delta \alpha) \times \nabla \beta - \nabla(\delta \beta) \times \nabla \alpha) d^3x \\ &= \frac{1}{4\pi} \int_S [\delta \alpha (\nabla \beta \times \vec{B}) - \delta \beta (\nabla \alpha \times \vec{B})] \cdot \vec{n} dS \\ &\quad + \frac{1}{4\pi} \int_V (\delta \alpha \nabla \beta \cdot \nabla \times \vec{B} - \delta \beta \nabla \alpha \cdot \nabla \times \vec{B}) d^3x. \end{aligned} \quad (2.49)$$

The surface integral vanishes since  $\alpha, \beta$  are fixed on  $S$ , i.e.  $\delta\alpha = \delta\beta = 0$  on  $S$ , and by setting  $\delta W = 0$  we obtain the equations

$$\nabla\alpha \cdot \nabla \times \vec{B} = 0, \quad \nabla\beta \cdot \nabla \times \vec{B} = 0,$$

i.e.

$$\vec{j} \cdot \nabla\alpha = 0, \quad \vec{j} \cdot \nabla\beta = 0,$$

which are just equations (2.22) and (2.23) specifying the force-free state. Hence equation (2.21) is satisfied, this is  $\vec{j} \times \vec{B} = 0$  as is expected.

So we may conclude from the variational principles that the force-free field is a state of stationary energy under the condition of a given flux distribution and connectivity of field lines. The current-free field is the absolute minimum-energy state under the condition of a given flux distribution.

### 3. NUMERICAL FORMULATION

#### 3.1. Iteration Formulation

We have recently begun to explore a new approach of computing general force-free magnetic fields. We imagine that a low-beta plasma is confined inside a volume  $V$ . We assume that the frozen-in condition is satisfied. We adopt the Clebsch variables  $\alpha$  and  $\beta$  to represent the magnetic field. The boundary condition is, therefore, decided by the given values of  $\alpha$  and  $\beta$  on the boundary surface  $S$ . We may set an initial field configuration which is required to fit the boundary conditions. If the initial field configuration is not force-free, as is most probably the case, field lines of this configuration would start to move with the plasma in the direction of the Lorentz force  $\vec{F}$ . As discussed in section 2.3, the Clebsch variable  $\alpha$  and  $\beta$  will be transported with the plasma unless the local Lorentz force vanishes. If we let the field relax step by step with time, we will obtain a series of magnetic field configurations, represented by different distributions of functions  $\alpha(\vec{r}, t)$ ,  $\beta(\vec{r}, t)$ , each obtained by correcting the  $\alpha, \beta$  values of the previous step with changes  $\delta\alpha$  and  $\delta\beta$  due to the displacement of field lines. Following this basic idea, we may formulate an iteration process for our numerical calculation of force-free field by using a finite-difference method.

We set the recursion formula

$$\begin{aligned}\alpha_{i,j}^{L+1} &= \alpha_{i,j}^L + \delta\alpha_{i,j}, \\ \beta_{i,j}^{L+1} &= \beta_{i,j}^L + \delta\beta_{i,j},\end{aligned}\tag{3.1}$$

where  $L$  is the number of iteration time internals, and  $(i, j)$  is the location of a mesh-point. Assuming that the displacement vector of a point on a line of force is  $\delta\vec{\xi}(\vec{r}, t)$ , the incremental terms can be written as

$$\begin{aligned}\delta\alpha &= -\delta\vec{\xi} \cdot \nabla\alpha, \\ \delta\beta &= -\delta\vec{\xi} \cdot \nabla\beta.\end{aligned}\tag{3.2}$$

We now suppose that the magnetic field is embedded in a highly conducting medium and that the parameters are such that the 'frozen-flux' condition is satisfied. However, we suppose that the system also contains a medium fixed in space, such that the plasma experiences a frictional force when it moves with respect to that medium. Then the equation of motion of the plasma is

$$\rho\left(\frac{\partial\vec{v}}{\partial t} + \vec{v} \cdot \nabla\vec{v}\right) = -\nabla p + \rho\vec{g} + \vec{F} - \nu\vec{v},\tag{3.3}$$

where  $\vec{F}$  again represents the Lorentz force,  $\rho$  and  $p$  are density and pressure,  $\vec{g}$  is the gravitational field, and  $\nu$  is the coefficient of friction. In the situations that lead to force-free fields,  $\rho$  and  $p$  are negligible, so that equation (3.3) leads to

$$\vec{v} = \nu^{-1}\vec{F}.\tag{3.4}$$

On combining equations (3.4) and (2.43), we obtain the equations

$$\begin{aligned}\frac{\partial\alpha}{\partial t} &= -\nu^{-1}\vec{F} \cdot \nabla\alpha, \\ \frac{\partial\beta}{\partial t} &= -\nu^{-1}\vec{F} \cdot \nabla\beta,\end{aligned}\tag{3.5}$$

where  $\nu$  is so far an arbitrary function of space and time. In practice, it has proved convenient to choose  $\nu$  so that equations (3.5) lead to the following increments

for  $\alpha$  and  $\beta$  for each time step :

$$\begin{aligned}\delta\alpha &= -\mu \frac{\vec{F} \cdot \nabla\alpha}{B^2}, \\ \delta\beta &= -\mu \frac{\vec{F} \cdot \nabla\beta}{B^2},\end{aligned}\tag{3.6}$$

where again  $\mu$  is an adjustable parameter. This so-called magneto-frictional method (Sturrock and Yang, 1985; Yang, Sturrock, and Antiochos, 1986), we find, is closely related to a method developed by Chodura and Schlüter (1980) for application to problems of three-dimensional magnetohydrostatic equilibria.

A stable numerical convergence by application of the finite difference method requires that the displacement of a point on a field line must be considerably smaller than the grid size, therefore, we suggest to take

$$\mu = \lambda(\Delta x_1, \Delta x_2)_{min}^2,\tag{3.7}$$

where  $\Delta x_1, \Delta x_2$  are grid sizes of a two-dimensional mesh,  $\lambda$  is a constant. Under this consideration, we rewrite the expressions for the increments of  $\alpha$  and  $\beta$  for each time step as :

$$\begin{aligned}\delta\alpha &= -\lambda_\alpha(\Delta x_1, \Delta x_2)_{min}^2 \frac{\vec{F} \cdot \nabla\alpha}{B^2}, \\ \delta\beta &= -\lambda_\beta(\Delta x_1, \Delta x_2)_{min}^2 \frac{\vec{F} \cdot \nabla\beta}{B^2},\end{aligned}\tag{3.8}$$

where  $\lambda_\alpha, \lambda_\beta$  are adjustable parameters.

The iteration forms expressed in equations (3.8), simple in appearance, have proved effective in practical computation of force-free magnetic fields. The parameters  $\lambda_\alpha$  and  $\lambda_\beta$  are generally less than unity. Larger  $\lambda_\alpha, \lambda_\beta$  may lead to



a faster convergence, but they must be limited so as not to exceed some critical values to avoid catastrophic numerical divergence. Practical experience tells us that  $\lambda_\alpha$ ,  $\lambda_\beta$  should reduce to smaller values when the field configuration is distorted further from the current-free state. In the following chapters we will show some examples of force-free fields calculated by application of the numerical method represented by equations (3.8).

The techniques represented by equations (2.24) and (3.8) for computing non-linear force-free fields appear to be quite different, yet this proves not to be the case. If we consider a rectangular coordinate system with equal mesh size  $h$ , Woodbury (1973) showed that the variations  $\delta\alpha$ ,  $\delta\beta$  required to satisfy equations (2.24) are given by

$$\begin{pmatrix} |\nabla\beta|^2 & -\nabla\alpha \cdot \nabla\beta \\ \nabla\alpha \cdot \nabla\beta & |\nabla\alpha|^2 \end{pmatrix} \begin{pmatrix} \delta\alpha \\ \delta\beta \end{pmatrix} = -\frac{h^2}{6} \begin{pmatrix} \vec{j} \cdot \nabla\beta \\ -\vec{j} \cdot \nabla\alpha \end{pmatrix}. \quad (3.9)$$

We find that the determinant of the matrix is given by

$$\Delta = |\nabla\alpha|^2 |\nabla\beta|^2 - (\nabla\alpha \cdot \nabla\beta)^2 = B^2, \quad (3.10)$$

so that equation (3.9) leads to

$$\begin{pmatrix} \delta\alpha \\ \delta\beta \end{pmatrix} = -\frac{h^2}{6B^2} \begin{pmatrix} |\nabla\alpha|^2 & \nabla\alpha \cdot \nabla\beta \\ -\nabla\alpha \cdot \nabla\beta & |\nabla\beta|^2 \end{pmatrix} \begin{pmatrix} \vec{j} \cdot \nabla\beta \\ -\vec{j} \cdot \nabla\alpha \end{pmatrix}. \quad (3.11)$$

This equation may be rewritten as

$$\begin{pmatrix} \delta\alpha \\ \delta\beta \end{pmatrix} = -\frac{h^2}{6B^2} \begin{pmatrix} \vec{F} \cdot \nabla\alpha \\ \vec{F} \cdot \nabla\beta \end{pmatrix}, \quad (3.12)$$

which is clearly of the same form as equations (3.8). Although the relaxation approach begins from quite different premises, it leads eventually to similar equations for computing force-free fields.

According to our magneto-frictional model, the field lines are continually doing work by magnetic force in moving against friction during the relaxation process. Since the only form to store energy is the magnetic field, we therefore expect that the field energy is continually decreasing. Let us assume that  $W$  is the total magnetic field energy stored in a volume  $V$ , then

$$W = \frac{1}{8\pi} \int_V B^2 d^3x, \quad (3.13)$$

while the decreasing rate of  $W$  can be written as

$$\frac{dW}{dt} = - \int_V \vec{v} \cdot \vec{F} d^3x. \quad (3.14)$$

On using equation (3.4), this becomes

$$\frac{dW}{dt} = - \int_V \nu^{-1} F^2 d^3x. \quad (3.15)$$

This confirms our conjecture that the total magnetic field energy will decrease monotonically, and that  $dW/dt = 0$  when  $\vec{F} = 0$  everywhere, this is, the magnetic field is force-free and a minimum-energy state.

### 3.2. Finite Difference Method

We consider a rectangular mesh on a surface  $S$  with coordinates  $x$  and  $z$ , on which the grid sizes are  $h_x$  and  $h_z$ , respectively. The values of the Clebsch

variables are given and fixed on the boundaries for a specified model concerned, and are also given inside the boundary as an initial field configuration. To perform the numerical iteration process, we need to calculate the magnetic field, electric current, Lorentz force, and then the increment terms of  $\alpha$  and  $\beta$  as seen in equations (3.8) from the first and second order derivatives of the Clebsch variables. For simplicity and economical satisfaction, we may use second order central differences for computing derivatives of each interior grid point. Assuming a two-dimensional scalar function, say  $f(x, z)$ , expressions for its first order derivatives are

$$\begin{aligned}\left(\frac{\partial f}{\partial x}\right)_{i,j} &= \frac{f_{i+1,j} - f_{i-1,j}}{2h_x} + 0(h_x^2), \\ \left(\frac{\partial f}{\partial z}\right)_{i,j} &= \frac{f_{i,j+1} - f_{i,j-1}}{2h_z} + 0(h_z^2),\end{aligned}\tag{3.16}$$

and expressions for its second order derivatives are

$$\begin{aligned}\left(\frac{\partial^2 f}{\partial x^2}\right)_{i,j} &= \frac{1}{h_x^2}(f_{i+1,j} - f_{i,j} + f_{i-1,j}) + 0(h_x^2), \\ \left(\frac{\partial^2 f}{\partial z^2}\right)_{i,j} &= \frac{1}{h_z^2}(f_{i,j+1} - f_{i,j} + f_{i,j-1}) + 0(h_z^2), \\ \left(\frac{\partial^2 f}{\partial x \partial z}\right)_{i,j} &= \frac{1}{4h_x h_z}(f_{i+1,j+1} - f_{i+1,j-1} - f_{i-1,j+1} + f_{i-1,j-1}) + 0(h_x h_z),\end{aligned}\tag{3.17}$$

where  $i$  and  $j$  are the grid numbers on the horizontal( $x$ ) and vertical( $z$ ) coordinates, respectively. In a two-dimensional case,  $(i, j)$  indicates the location of a corresponding grid point.

For a force-free field, the electric current must be parallel to the magnetic field. This can be checked by estimating the angle between  $\vec{j}$  and  $\vec{B}$  at each

mesh point,

$$\vartheta_{i,j} = \cos^{-1} \frac{|\vec{j}_{i,j} \cdot \vec{B}_{i,j}|}{|\vec{j}_{i,j}| |\vec{B}_{i,j}|}, \quad (3.18)$$

which should approach to zero everywhere during the iteration process. Note that if  $\vec{j} \cdot \vec{B} > 0$ ,  $\vec{j}$  is nearly parallel with  $\vec{B}$ ; while  $\vec{j} \cdot \vec{B} < 0$ ,  $\vec{j}$  is nearly anti-parallel with  $\vec{B}$ .

In this numerical method the total magnetic field energy is calculated by summing up the field energy stored in individual cells, in each of which field strength is taken to be that at the center of that cell, i.e.

$$W = \sum_{i,j} \frac{B_{i,j}^2}{8\pi} \Delta V_{i,j}. \quad (3.19)$$

According to the variational principles discussed in the previous sections, performance of this numerical method can also be monitored by estimating the field energy, which is expected to decrease monotonically and approach asymptotically a minimum-energy state.

### 3.3. Adjustable Grid Sizes

The weakness of the finite difference method with using constant grid size, as described above, is that the grid size must be chosen quite small in order to attain appropriate accuracy. It would be very expensive in computing time if the calculation is run directly on a mesh with a large number of grid points. This is not only because we have to compute various physical parameters on a large number of grid points during each iteration, but also because the displacement

vectors,  $\vec{\xi}$ , as seen in equation (3.2), have to take small values and therefore lead to a very slow convergence of the magnetic field lines. For many astrophysical cases, we must calculate a force-free magnetic field over a very large scale, for example, to simulate coronal magnetic field configurations in a half-space domain. Calculation with constant grid size proves uneconomical and even unacceptable. To overcome this difficulty, we adopt methods with adjustable grid sizes.

(a) Multigrid Method

It is advantageous to begin with a coarse mesh that can lead a fast convergence and get rid of perturbations of large wave number in a reasonable number of time steps. We then choose successively smaller grid sizes to continue the computation and obtain a solution with higher accuracy. A straightforward way is to simply divide each grid size into halves, i.e.  $h_{x2} = 0.5 h_{x1}$  and  $h_{z2} = 0.5 h_{z1}$ , so that the mesh number increases from  $N1 \times N1$  to  $N2 \times N2$ , where  $N2 = 2N1$ . Note that the horizontal mesh number and the vertical mesh number could be chosen to be unequal.

Let us assume that  $f_{m,n}^{(1)}$  is the calculated value of a function  $f(x, z)$  at grid point  $(m, n)$  on the coarse mesh, and  $f_{i,j}^{(2)}$  is the expected value for  $f(x, z)$  at grid point  $(i, j)$  on the finer mesh. At any point on the re-gridded mesh that does not overlap a grid point of the coarse mesh,  $f_{i,j}^{(2)}$  can be estimated by numerical interpolation for the midpoint on the coarse mesh. For example, the grid point  $(2m, 2n - 1)$  on the finer mesh is located at the midpoint be-

tween  $(m, n)$  and  $(m + 1, n)$  on the coarse mesh. By using the Lagrange four point interpolation formula, the value of  $f(x, z)$  at that point is estimated to be

$$f_{2m, 2n-1}^{(2)} = -\frac{1}{16}f_{m-1, n}^{(1)} + \frac{9}{16}f_{m, n}^{(1)} + \frac{9}{16}f_{m+1, n}^{(1)} - \frac{1}{16}f_{m+2, n}^{(1)} + O(h_{x1}^4). \quad (3.20)$$

If  $i = 2$ , i.e. the first grid point next to the  $x = 0$  boundary on the finer mesh, the  $f$ -function can be estimated by a Lagrange three point interpolation formula

$$f_{2, 2n-1}^{(2)} = \frac{3}{8}f_{1, n}^{(1)} + \frac{3}{4}f_{2, n}^{(1)} + \frac{1}{8}f_{3, n}^{(1)}. \quad (3.21)$$

Remember that the iteration on the re-gridded mesh will take small increments for the Clebsch variables as could be seen from equations (3.8). However, since the convergence of field lines now starts at an 'almost' force-free state, it will go rapidly and smoothly to a higher order of accuracy. For the situation requiring further high accuracy, one may regrid the mesh and repeat the iteration process again, and so forth. This multigrid method is found to be highly advantageous in our calculations. Examples will be shown in the following chapters.

#### (b) Adaptive-Grid Technique

In the case of considering a force-free field with infinite boundaries, one has numerically to extend the boundaries of the computing mesh to be as large as the computation capacity allows in order to simulate the real physical case. The

fact we know is that highly stressed field lines may inflate, moving towards an open-field configuration. The artificial pressure due to a finite numerical boundary may badly distort the outer field lines, and lead to an unacceptable result because of large errors introduced. If we set a mesh of very large scale and do not want to miss the fine structure in the strong field region, the required grid number could be too large for the capacity of our computer (VAX 750) even if a multigrid method were applied. One possible solution to this shortcoming is to adopt a larger mesh sizes in the weak-field region, so that the total number of grids will be reduced without losing fine structures in the strong-field region.

Figure 4 shows panels with variable sizes on a two-dimensional rectangular map. The expressions for the first and second order derivatives of the Clebsch variables at each grid point can be computed by some linear interpolation technique, which are a little more complicated than those used for uniform meshes which are presented in equations (3.16) and (3.17).

We may still assume a scalar function  $f(x, z)$ , and introduce parameters defined by

$$\begin{aligned} p_x^{(i)} &\equiv \frac{\Delta x_{i-1}}{\Delta x_{i-1} + \Delta x_i}, \\ p_z^{(j)} &\equiv \frac{\Delta z_{j-1}}{\Delta z_{j-1} + \Delta z_j}, \end{aligned} \tag{3.22}$$

where  $\Delta x_{i-1}$ ,  $\Delta x_i$ ,  $\Delta z_{j-1}$ , and  $\Delta z_j$  are grid sizes as shown in Figure 4. For a mesh with increasing grid size, we have  $p_x^{(i)}, p_z^{(j)} < 0.5$ , for  $i, j > 2$ .

The first order derivatives may be computed by

$$\begin{aligned} \left(\frac{\partial f}{\partial x}\right)_{i,j} &= \frac{1-p_x^{(i)}}{\Delta x_{i-1}}(f_{i,j} - f_{i-1,j}) + \frac{p_x^{(i)}}{\Delta x_i}(f_{i+1,j} - f_{i,j}), \\ \left(\frac{\partial f}{\partial z}\right)_{i,j} &= \frac{1-p_z^{(j)}}{\Delta z_{j-1}}(f_{i,j} - f_{i,j-1}) + \frac{p_z^{(j)}}{\Delta z_j}(f_{i,j+1} - f_{i,j}), \end{aligned} \quad (3.23)$$

which can also be written in the following forms

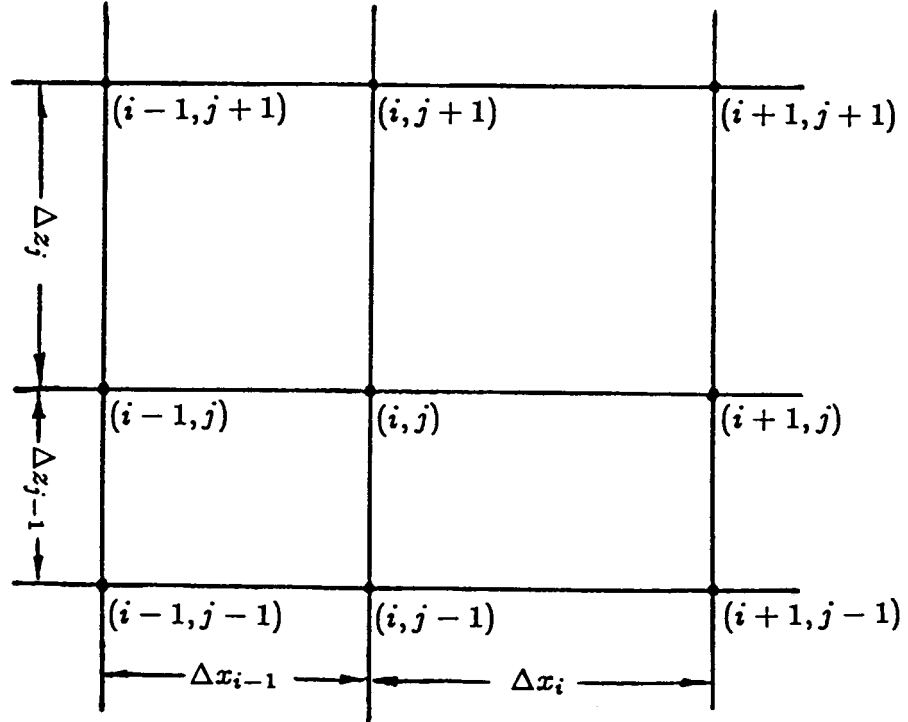


Figure 4. Illustration of panels with varying sizes.



$$\begin{aligned}
\left(\frac{\partial f}{\partial x}\right)_{i,j} &= \frac{p_x^{(i)}}{\Delta x_i} f_{i+1,j} + \left(\frac{1}{\Delta x_{i-1}} - \frac{1}{\Delta x_i}\right) f_{i,j} - \frac{1-p_x^{(i)}}{\Delta x_{i-1}} f_{i-1,j}, \\
\left(\frac{\partial f}{\partial z}\right)_{i,j} &= \frac{p_z^{(j)}}{\Delta z_j} f_{i,j+1} + \left(\frac{1}{\Delta z_{j-1}} - \frac{1}{\Delta z_j}\right) f_{i,j} - \frac{1-p_z^{(j)}}{\Delta z_{j-1}} f_{i,j-1}.
\end{aligned} \tag{3.24}$$

And we may apply the following forms for computing the secondary derivatives

$$\begin{aligned}
\left(\frac{\partial^2 f}{\partial x^2}\right)_{i,j} &= \frac{2}{(\Delta x_{i-1} + \Delta x_i)^2} \left( \frac{1}{1-p_x^{(i)}} f_{i+1,j} - \frac{1}{p_x^{(i)}(1-p_x^{(i)})} f_{i,j} + \frac{1}{p_x^{(i)}} f_{i-1,j} \right), \\
\left(\frac{\partial^2 f}{\partial z^2}\right)_{i,j} &= \frac{2}{(\Delta z_{j-1} + \Delta z_j)^2} \left( \frac{1}{1-p_z^{(j)}} f_{i,j+1} - \frac{1}{p_z^{(j)}(1-p_z^{(j)})} f_{i,j} + \frac{1}{p_z^{(j)}} f_{i,j-1} \right), \\
\left(\frac{\partial^2 f}{\partial x \partial z}\right)_{i,j} &= \frac{p_z^{(j)}}{\Delta z_j} \left(\frac{\partial f}{\partial x}\right)_{i,j+1} + \left(\frac{1}{\Delta z_{j-1}} - \frac{1}{\Delta z_j}\right) \left(\frac{\partial f}{\partial x}\right)_{i,j} - \frac{1-p_z^{(j)}}{\Delta z_{j-1}} \left(\frac{\partial f}{\partial x}\right)_{i,j-1}.
\end{aligned} \tag{3.25}$$

In practice one may find that it is much advantageous to compute force-free field problems by using a multi-grid method on a mesh with variable grid sizes.

### (c) Spherical Coordinates

It is convenient to treat problems such as magnetic dipole fields in a spherical coordinate system. We may arrange the increment in radius to be increasing with the radius, so the mesh will have larger grid sizes in the remote weak field region. Expressions for derivatives of the Clebsch variables could be obtained in a way similar to what is shown in section 3.3 (b).

We have computed some force-free field problems on spherical coordinates. Results showed fast convergence of magnetic field energy. Computing with spher-

ical coordinates is an appropriate way for studying large scale force-free magnetic fields.

There are two shortcomings for the use of spherical coordinate systems. One is that numerical formulae for computing physical items, such as magnetic field, current, and magnetic force, are not as neat as in a rectangular coordinate system. The second is that one has to create a subroutine to plot the contours of field lines.

#### 4. TEST MODEL

We may start our calculation for some two-dimensional models in a rectangular coordinate system. To construct a magnetic field, say  $\vec{B}(x, z)$ , we assume that the Clebsch variables have the forms

$$\begin{aligned}\alpha &= \alpha(x, z), \\ \beta &= \beta(x, y, z) = y - \gamma(x, z).\end{aligned}\tag{4.1}$$

Following definition (2.18), we have

$$\begin{aligned}B_x &= -\frac{\partial \alpha}{\partial z}, \\ B_y &= \frac{\partial \alpha}{\partial x} \frac{\partial \gamma}{\partial z} - \frac{\partial \alpha}{\partial z} \frac{\partial \gamma}{\partial x}, \\ B_z &= \frac{\partial \alpha}{\partial x}.\end{aligned}\tag{4.2}$$

Since the magnetic field is independent of  $y$ , the field configuration defined by equations (4.1) is determined by  $\alpha(x, z)$  and  $\gamma(x, z)$ . We find that the effect of the scalar function  $\gamma(x, z)$  is only on the  $B_y$ -component. If  $\gamma = \text{constant}$  everywhere, then  $B_y$  vanishes everywhere. We may consider that the function  $\gamma(x, z)$  represents displacement of field lines in the  $y$ -direction. The representation of equations (4.1) is quite convenient for us to study the evolution of a force-free magnetic field due to the shift of the footpoints of field lines. This kind of shift, for example on the  $x - y$  plane, can be easily represented by the values of  $\gamma(x, 0)$ .

If  $\Phi(x, z)$  is the magnetic flux embraced by  $x = x_0, x$ , and  $y = y_1, y_1 + \Delta y$ ,

then we have

$$\begin{aligned}
 \Phi(x, z) &= \Delta y \int_{x_0}^x B_z dx \\
 &= \Delta y \int_{x_0}^x \frac{\partial \alpha}{\partial x} dx \\
 &= \Delta y (\alpha(x, z) - \alpha(x_0, z)),
 \end{aligned} \tag{4.3}$$

or we have

$$\frac{\Phi(x, z)}{\Delta y} = \alpha(x, z), \tag{4.4}$$

provided that  $\alpha(x_0, z) = 0$ . Hence  $\alpha$  is a measure of magnetic flux.

In order to study the variation, during the iteration process, of the departure of the calculated magnetic field from the force-free field, it was convenient to base a test case on an already known force-free configuration. The following functional forms for  $\alpha$  and  $\beta$

$$\begin{aligned}
 \alpha(x, z) &= -\frac{B_0}{k} e^{-lz} \cos kx, \\
 \beta(x, y, z) &= y - \gamma(x, z) = y - \left(\frac{k^2}{l^2} - 1\right)^{1/2} x
 \end{aligned} \tag{4.5}$$

yield the field configuration

$$\begin{aligned}
 B_x &= -\frac{l}{k} B_0 e^{-lz} \cos kx, \\
 B_y &= -\left(1 - \frac{l^2}{k^2}\right)^{1/2} B_0 e^{-lz} \cos kx, \\
 B_z &= B_0 e^{-lz} \sin kx,
 \end{aligned} \tag{4.6}$$

where  $B_0, l, k$  are constants; and (4.6) is readily shown to be force-free for  $l \leq k$ .

This field configuration is periodic in the  $x$ -direction, but a section of it may provide a simple model for a coronal arcade of lateral extent  $\pi/k$  (Priest

1982). The shear angle  $\chi$ , which defines the inclination of the field lines to the  $x$ -direction, is

$$\chi = \tan^{-1} \left( \frac{k^2}{l^2} - 1 \right)^{\frac{1}{2}} \quad (4.7)$$

at their summits. It is easy to see that when  $l = k$ , then  $\chi = 0$ , and  $\gamma(x, z)$  vanishes, so that we have a current-free field

$$B_x = -B_0 e^{-kz} \cos kx, \quad B_y = 0, \quad B_z = B_0 e^{-kz} \sin kx. \quad (4.8)$$

As  $l$  decreases from  $k$  to 0, the shear angle  $\chi$  increases from 0 to  $\frac{\pi}{2}$ . Also we find

$$\nabla \times \vec{B} = (k^2 - l^2)^{\frac{1}{2}} \vec{B}, \quad (4.9)$$

so that this field model is a constant- $\lambda$  force-free field as we discussed in Chapter 1, when  $\lambda = (k^2 - l^2)^{\frac{1}{2}}$ .

The projections of the magnetic field lines of this field model on the  $x - z$  and  $x - y$  planes are shown in Figure 5, where we adopted  $B_0 = 2.0$ ,  $k = 1.0$ , and  $l = 0.8$ . It is clear that the projections of field lines on the  $x - z$  plane are just the constant- $\alpha$  contours, while the projections of field lines on the  $x - y$  plane can be represented by constant- $\beta$  contours on that plane. The numbers labeled on those contours represent the  $\alpha$  (see the upper figure) and  $\beta$  (see the lower figure) values respectively, which specify field lines individually by pairs of  $(\alpha, \beta)$ .

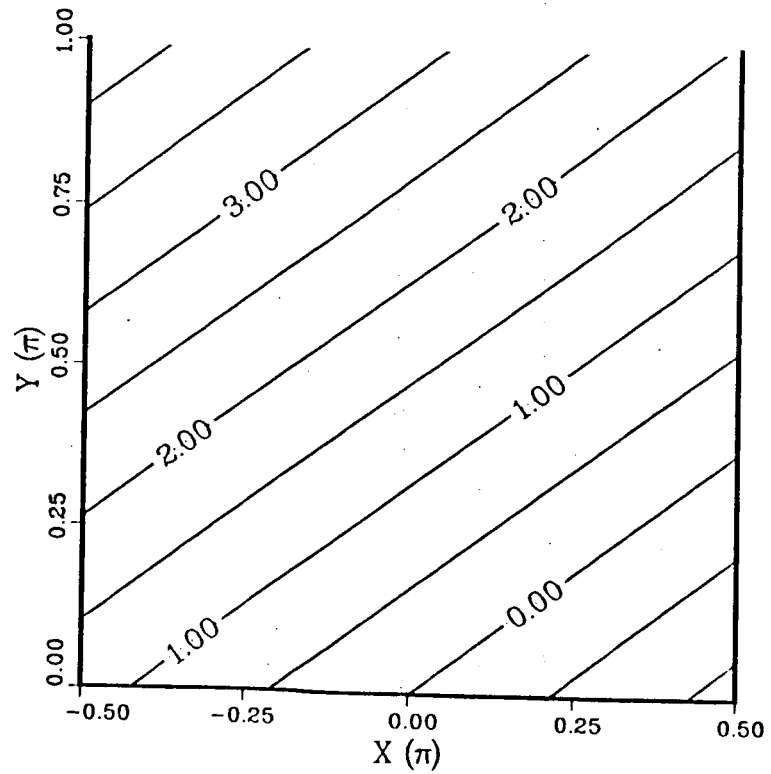
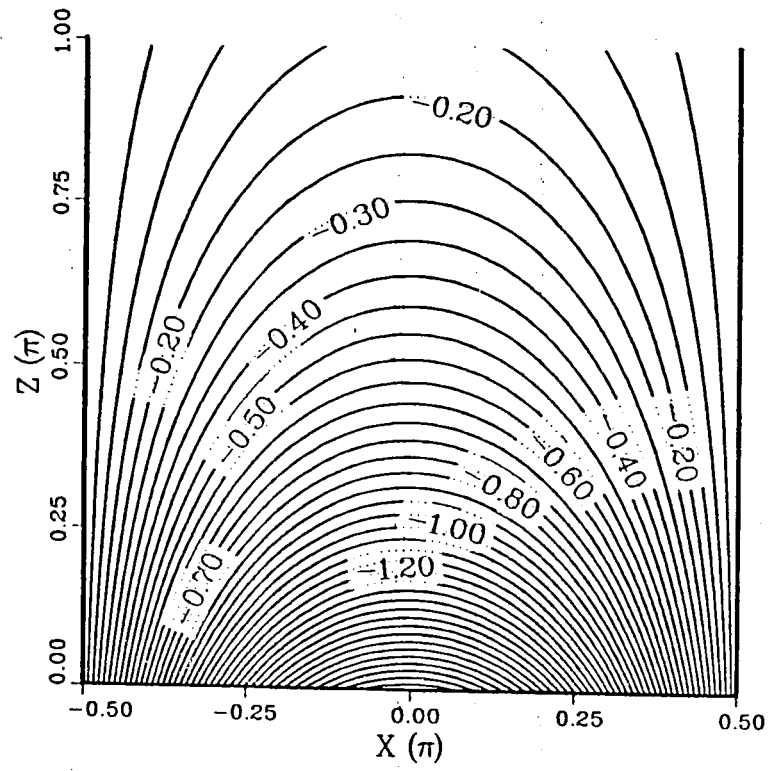


Figure 5. Vertical and horizontal sections through a force-free magnetic configuration described by equation (4.6) with  $B_0 = 2.0$ ,  $k = 1.0$ , and  $l = 0.8$ .

We now set a rectangular boundary on the  $x - z$  plane of size  $\pi/2 \times \pi/2$ , and added large perturbations

$$\begin{aligned}\Delta\alpha &= -\sin 2x \sin 2z, \\ \Delta\gamma &= 0.4 \sin 2x \sin 2z\end{aligned}\tag{4.10}$$

to the force-free forms of  $\alpha(x, z)$ ,  $\gamma(x, z)$ , as shown in equations (4.5). We take this as an initial trial function. We may note that since  $\Delta\alpha$  and  $\Delta\gamma$  both vanish on the boundary, the field lines, though largely distorted inside the boundary, will have the same connection with the bounding surface as the force-free field. The values of  $\alpha$  and  $\gamma$  on the boundaries were always fixed during the relaxation process, when we applied the iteration forms (3.8) to the grid points inside the boundaries. By noting that  $\nabla\beta = \hat{y} - \nabla\gamma$ , we may write the increments of  $\alpha$ ,  $\gamma$  for iteration performance as

$$\begin{aligned}\delta\alpha_{i,j} &= -\lambda_\alpha h_x h_z \left( F_x \frac{\partial\alpha}{\partial x} + F_z \frac{\partial\alpha}{\partial z} \right)_{i,j}, \\ \delta\gamma_{i,j} &= -\lambda_\gamma h_x h_z \left( F_x \frac{\partial\gamma}{\partial x} - F_y + F_z \frac{\partial\gamma}{\partial z} \right)_{i,j},\end{aligned}\tag{4.11}$$

where  $F_x$ ,  $F_y$ ,  $F_z$  are components of the magnetic force calculated by the finite-difference method.

To check the computation performance, we plotted the *constant*  $-\alpha$  and the *constant*  $-\gamma$  contours to compare with the force-free forms, and also estimated the magnetic field, the current, the Lorentz force, and the angle between the field and the current at each grid point during the iteration process to ensure that the magnetic field configuration was converging to a force-free state.

We first applied a very coarse mesh ( $8 \times 8$ ) to the case, on which iteration was performed about 60 times. The convergence of field lines represented by a series of  $\alpha$ -contours and  $\gamma$ -contours during the iteration process is shown in Figure 6. The initial field configuration is shown in Figure 6(a), on which we may see that field lines are distorted by a large amount from the force-free state and that there appears a magnetic island in the  $\alpha$ -contours. We also show the forms of the potentials of  $\alpha$  and  $\gamma$  after 5, 10, and 60 iterations on Figure 6 (b, c, d), respectively. From those figures we may see that the field lines converge quite rapidly during the first few steps because of the large initial magnetic force. Then they move smoothly towards a stable state, since the magnetic force becomes smaller and smaller when the magnetic field is close to a force-free configuration.

Figure 6(d) is very close to the exact solution, as we compare the computed  $\alpha(x, z)$  and  $\gamma(x, z)$  with the corresponding values of the analytical force-free forms. And the Lorentz force of this field configuration differs from zero by only  $10^{-3}$  of its initial magnitude. The average angle between current and the magnetic field in the initial field is  $\bar{\vartheta}_0 \simeq 82^\circ$ . After 60 times of iteration it reduces to  $\bar{\vartheta}_{60} \simeq 0.8^\circ$ , and  $\vartheta_{i,j}$  is less than  $0.1^\circ$  in the strong field region, so that the current is nearly parallel with the magnetic field. This calculation takes only a few seconds on a VAX/750.



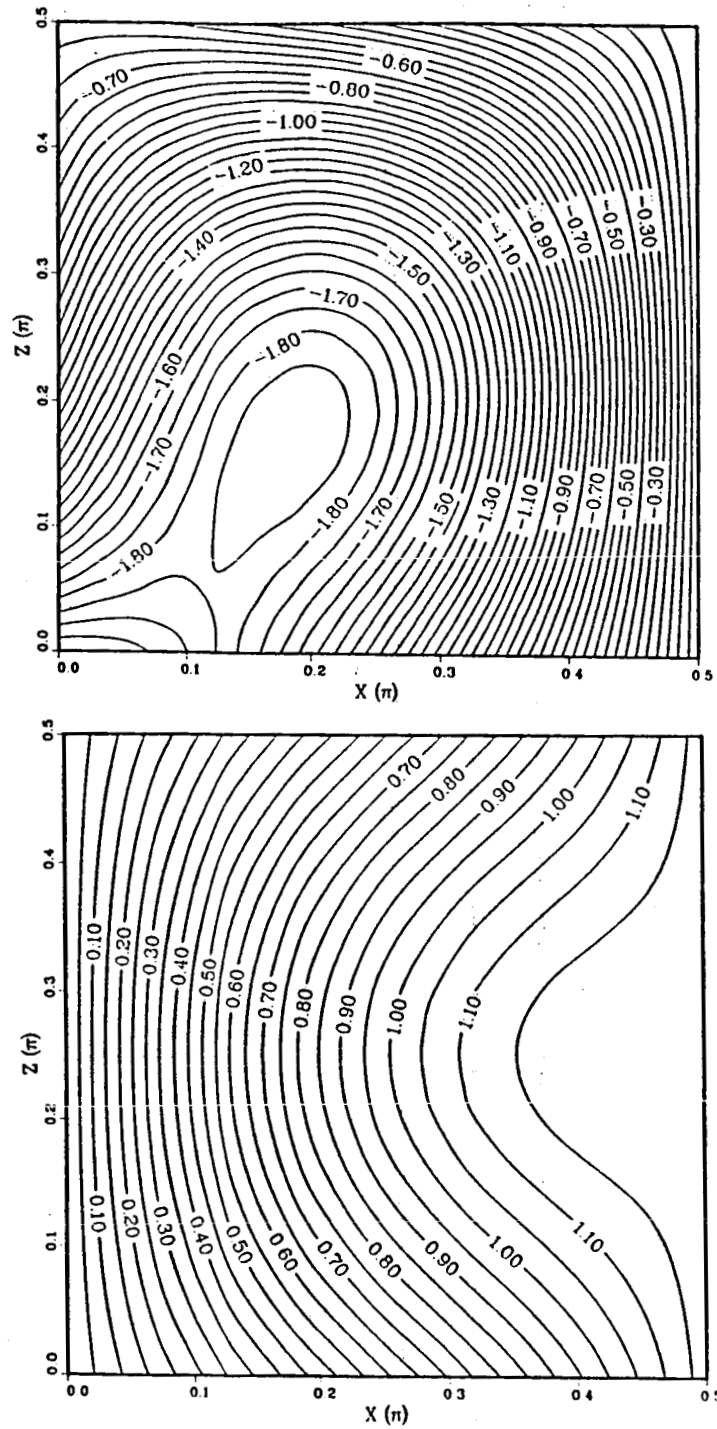
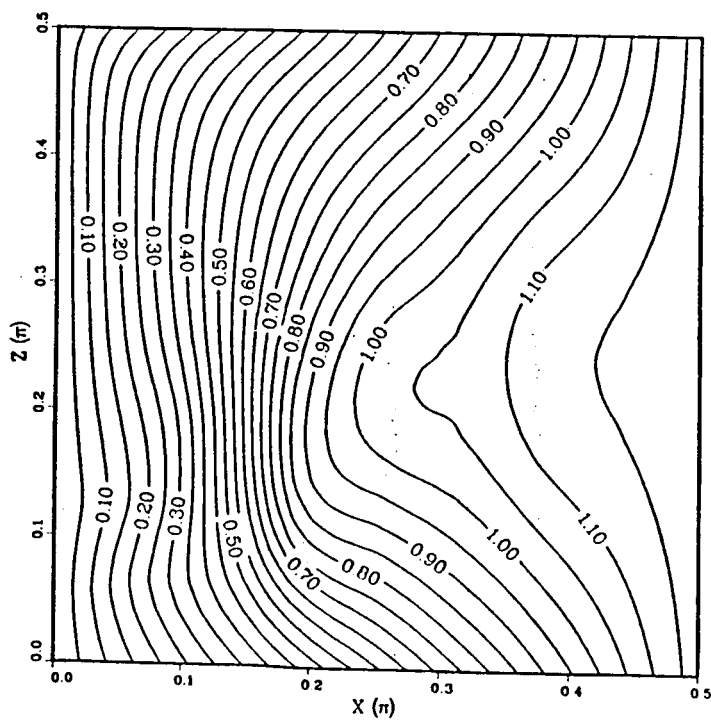
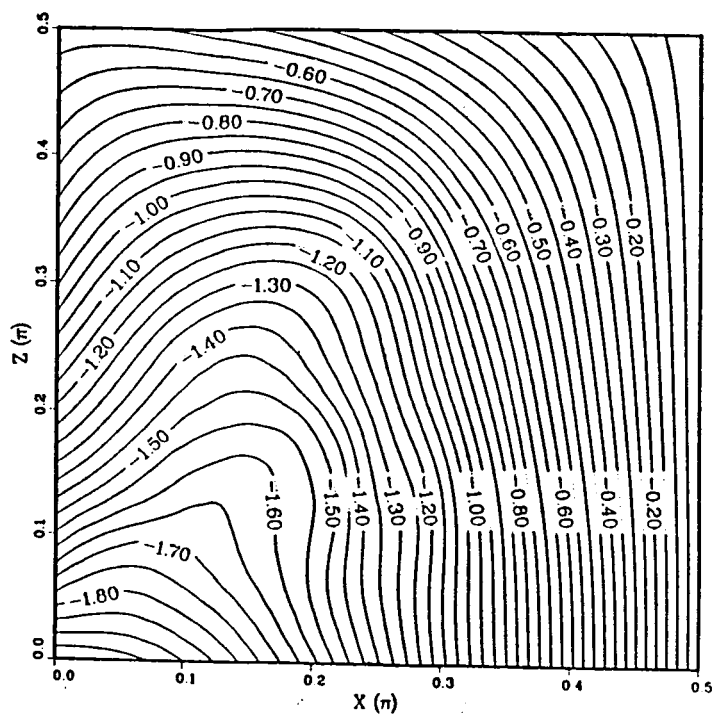
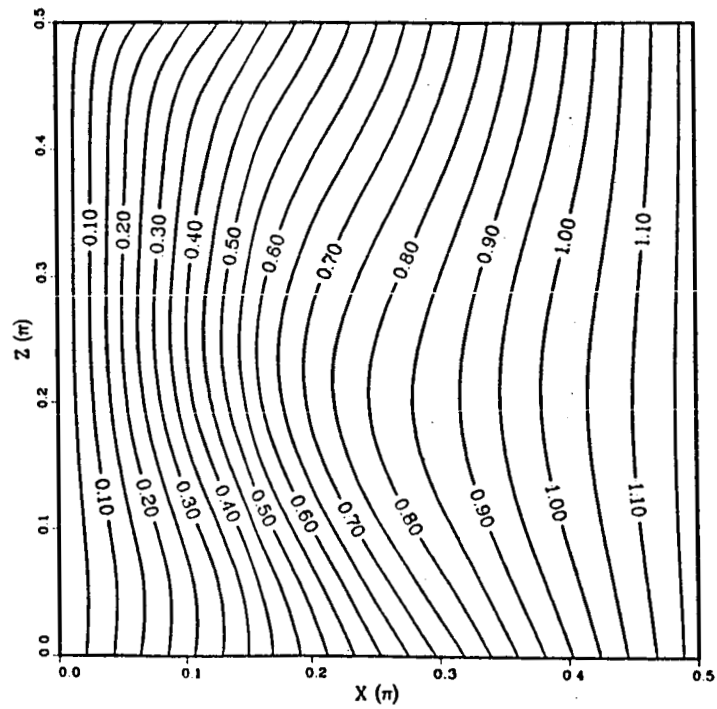
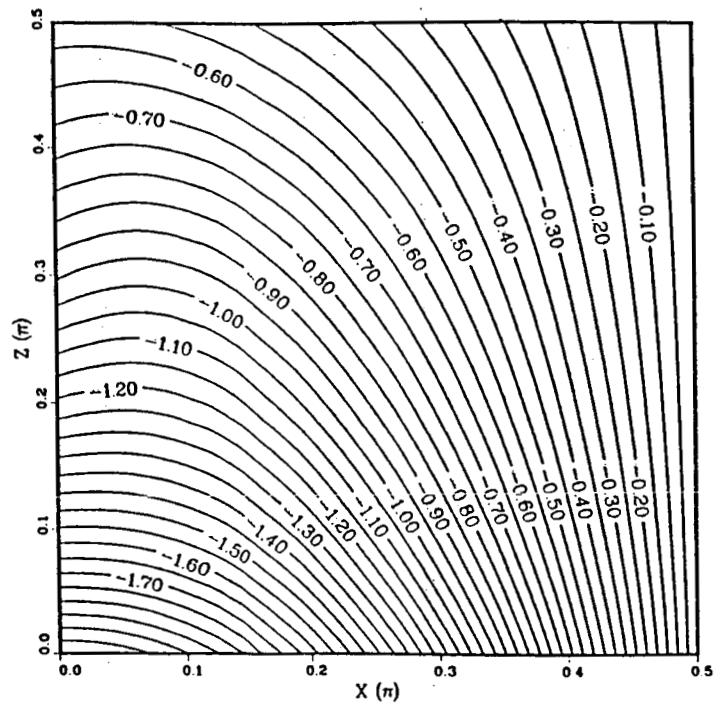


Figure 6. Contours of constant- $\alpha$  (projection of field lines) and constant- $\gamma$  for two dimensional problem described in chapter 4. Calculation was performed on a very coarse mesh ( $8 \times 8$ ).

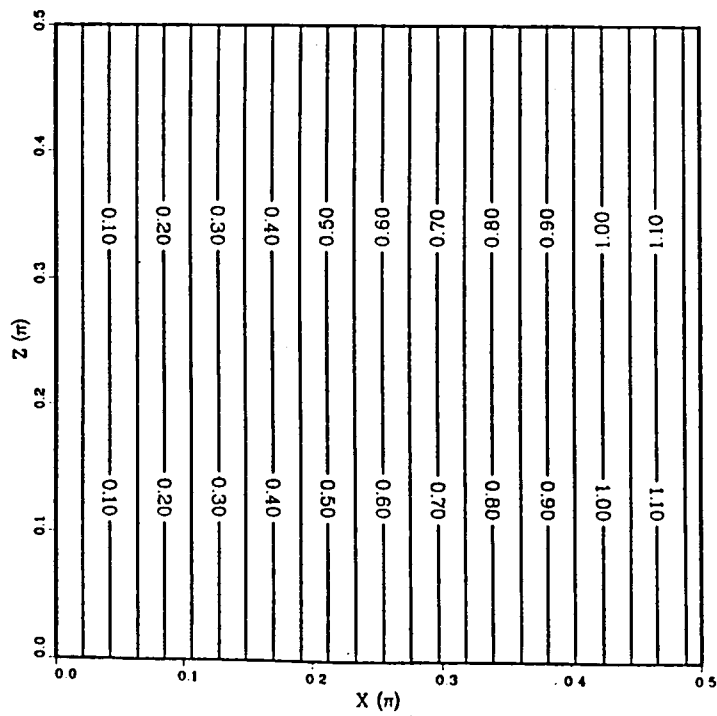
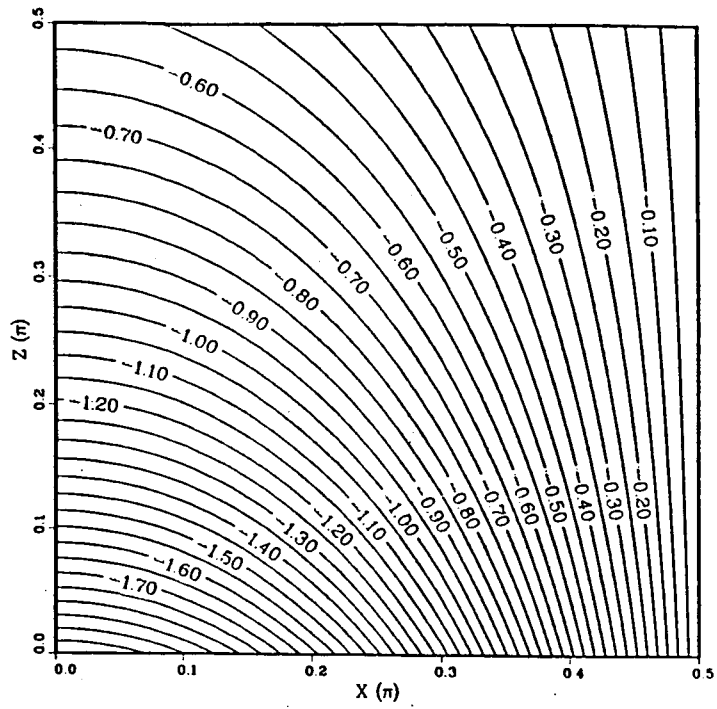
(a) the assumed initial field configuration.



(b) field configuration after 5 iterations.



(c) field configuration after 15 iterations.



(d) field configuration after 60 iterations.

Figure 7 is a plot of the variation of the excess of the estimated magnetic energy over its exact value (calculated by the analytical solution) as the iteration proceeds. The magnetic field energy  $W$  in the initial trial configuration is about 2.6 times of the force-free field energy  $W_0$ . We see that  $W$  converges to  $W_0$  nearly exponentially during the iteration process. This is just what we expect for our method.

To obtain high order of accuracies, we may adopt finer meshes successively. This multigrid method has been described in Chapter 3. We list the results of calculation of the test model on a  $8 \times 8$  mesh, then on a regridded  $16 \times 16$  mesh, and on a  $32 \times 32$  mesh in Table 1.

TABLE 1  
RESULTS OF MULTIGRID METHOD  
ON TEST MODEL

Mesh	Iteration	$W$	$\bar{\vartheta}(^{\circ})$
$8 \times 8$	0	9.28244	81.5
	60	3.58585	0.79
$16 \times 16$	0	3.60313	2.60
	60	3.60311	0.22
$32 \times 32$	0	3.60745	0.64
	60	3.60745	0.16

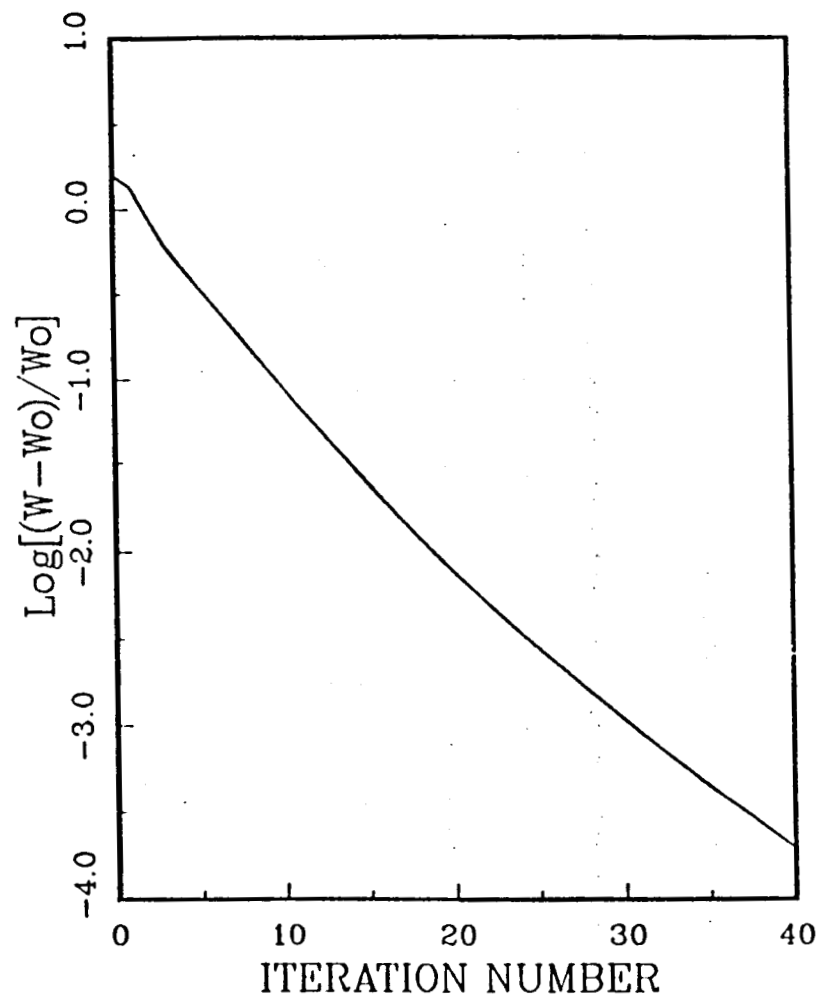


Figure 7. The excess energy of the computed force-free field over the energy of the exact field, as a function of iteration number, for the case described in Chapter 4.

From the results in Table 1, we see that the magnetic field energy is almost stable during the iteration process on the finer meshes. The field energies on the  $16 \times 16$  mesh and on the  $32 \times 32$  mesh are very close or just equal to the exact value one can obtain by substituting the Clebsch variables of the analytical force-free forms. The small change in the average angle between the current and the magnetic field,  $\bar{\vartheta}$ , indicates slight alignment of the electric current with the magnetic field in the weak field region. The advantage of the multigrid method is quite distinctive if we compare the above calculation with that by applying the fine mesh directly. To obtain a result with similar accuracy as that listed in Table 1 may take more than one thousand iteration times if calculated directly on a  $16 \times 16$  mesh. One may also find that it is very difficult to converge the field configuration with such a large initial perturbation into a force-free solution by adopting a  $32 \times 32$  mesh directly.

The purpose of setting the initial field configuration with perturbation (4.10) is to investigate how the method works in case that the initial field is far from the force-free solution. One of the key points of this method is the moving of field lines in the direction of the magnetic force. The topology of the magnetic field may change, the total magnetic field energy decreases, and the excess field energy is dissipating numerically during the iteration process. In particular, the magnetic island shown in Figure 6(a) disappears from later configurations. Such changes can occur only if reconnection of field lines is taking place. Although the equations that are the basis of our model do not pro-

vide for reconnection, the implement of our numerical technique involves finite-difference approximations to the differential equations. The finite-difference representation involves 'numerical dissipation' that permits reconnection. It is clear that this 'numerical dissipation' is quite large in the case that we adopt a coarse mesh, since the field lines are allowed to displace a large step towards a lower energy configuration during each iteration. This kind of displacement may connect field lines with same labels and swallow the magnetic island. What we are interested is the final force-free solution of lowest energy, so the large 'numerical dissipation' is a benefit in providing a rapid convergence.

The reader may worry about whether the large 'numerical dissipation' could lead to potential field instead of a force-free field. It will not in general be the case, since the field configuration must be compatible with the boundary conditions on the Clebsch variables that specify the magnetic connectivity.

From the calculation of the test model, we may conclude that this method leads to the particular force-free state with prescribed connectivity of the magnetic field at the bounding surface, and with minimum energy. From the experiments done to date, it appears that the topology that has lowest energy is also the simplest topology.



## 5. ROTATIONAL SUNSPOT MODEL

### 5.1. Solar Flares and Magnetic Fields

Solar flares are energetic phenomena in solar active regions, which emit electromagnetic radiations with a very broad range of wavelengths, in extreme cases from  $0.002\text{\AA}$  up to more than  $10\text{km}$  (Švestka 1976). Individual solar flares differ greatly in size and energy released. What is common to all of them is a rapid temporary heating of a restricted part of the solar corona and chromosphere. Depending upon the magnetic configuration, non-thermal processes may also occur at some places inside the flaring volume giving rise to accelerated electrons and atomic nuclei. The accelerated electrons manifest themselves through impulsive non-thermal  $X$ -ray and radio bursts which occur during the rising phase of the flare development. In some flares the non-thermal component is dominant. The accelerated particles, traveling into interplanetary space, may give rise to geomagnetospheric storms and brighten the aurora in polar regions. Observations have found limb flares associated with the high-speed ejection of flare matter.

From the statistical analysis of the observational data, it may be concluded that all solar flares occur in active regions characterized by sunspots, plages, and often quiescent filaments. By far the most flares occur in active regions with developed sunspots. Flares which appear in an active region without spots are exceptional events. Magnetic changes close to the zero

line (the longitudinal component  $B_{\parallel} = 0$ ) appear to be of great importance for flare occurrence. Changes there may be due to emergence of new flux, as well as to deformations of field caused by motions and rotations of sunspots. According to Sakurai (1972), a necessary condition for the occurrence of major flares is a substantial increase of the gradient of the magnetic field, while high gradients are most likely to occur in a sunspot group with rotating motion.

The total energy released by flare processes has been estimated to be in range of  $10^{28} - 10^{32}$  *ergs*, which is generally believed to be stored in magnetic form before the onset of a flare event. If the initial flare volume is  $V$ , the energy  $W$  is gained when the field strength  $B$  decreases by

$$\Delta(B^2) = 8\pi W/V. \quad (5.1)$$

Thus for example for  $V = 10^{28} \text{ cm}^3$ , a decrease of only  $0.03 - 270$  *G* is required for  $W \sim 10^{28} - 10^{32}$  *ergs* in a field originally of  $600$  *G*. This shows that in principle flares can derive their energy from the magnetic field.

In consideration of observations (Sweet, 1969; Sturrock, 1980), it seems plausible to accept the storage of magnetic energy by departure from a potential field, since the potential field represents the minimum energy state with no extractable energy. Then in view of the lack of apparent motions in the solar atmosphere before flares, the energy storage in force-free magnetic fields becomes of particular interest. As a practical example, Barnes and Sturrock (1972) have considered a sunspot of one polarity

surrounded by a magnetic field region of opposite polarity. Without any initial twisting the magnetic field has a current-free configuration. Then, however, the sunspot begins to rotate in consequence of differential rotation. The magnetic field configuration develops currents, but, because of the low plasma density, the field adopts a force-free structure. The energy stored in the magnetic field will then increase as the rotation angle increases. Their calculation was carried out for a cylindrically symmetric model by applying a relaxation method as we have mentioned in Chapter 2.

Figure 8 ( Nakagawa et al., 1971) shows a spiral topology of chromospheric fibrils and filaments observed in  $H_\alpha$  near sunspots and the configuration of axisymmetric force-free magnetic lines of force. The field configuration resembles the situation Barnes and Sturrock considered.

## 5.2. Modified Barnes-Sturrock Model

In this section the particular field model we will consider is one of cylindrical symmetry. If we introduce cylindrical coordinates  $r, \theta, z$ , the magnetic field configuration  $\vec{B}(r, z)$  may be represented by the two Clebsch variables in the forms

$$\begin{aligned}\alpha &= \alpha(r, z), \\ \beta &= \theta - \gamma(r, z),\end{aligned}\tag{5.2}$$

where the scalar function  $\gamma(r, z)$  traces the variation of  $\theta$  along a field line, since  $\beta = \text{const.}$  on a field line.

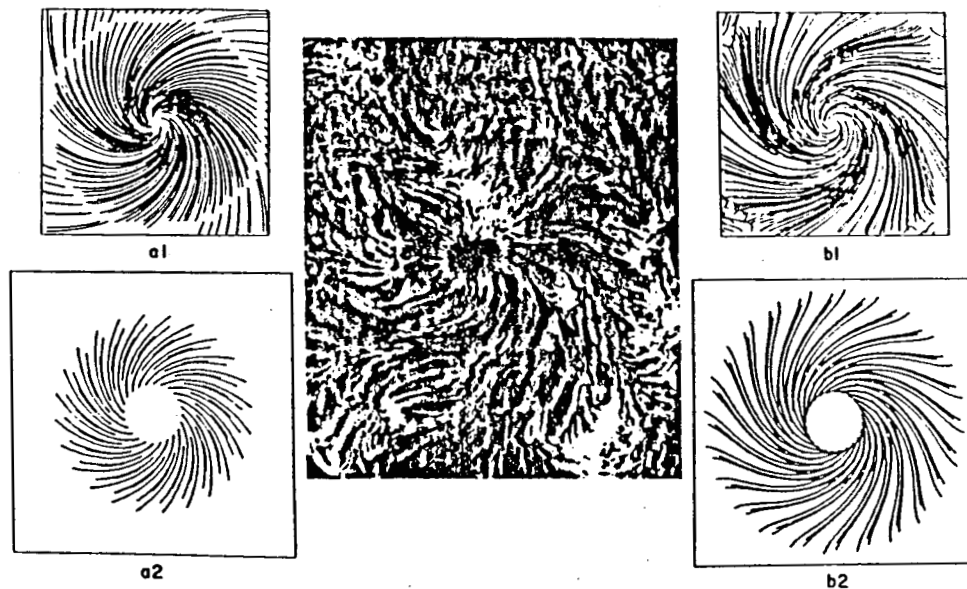


Figure 8. An example of spiral topology of filaments near a sunspot in  $H_{\alpha}$  observation (Big Bear Observatory, 9 September 1970) and the configuration of lines of force of force-free magnetic fields; a1, a2 the  $B^{(0)}$ -field (the simplest solution) and b1, b2 the  $B^{(1)}$ -field (the next solution) for the spiral angle  $45^{\circ}$  (Nakagawa et al., 1971).

The gradients of  $\alpha$ ,  $\beta$  in cylindrical coordinates are

$$\begin{aligned}\nabla\alpha &= \frac{\partial\alpha}{\partial r}\hat{r} + \frac{\partial\alpha}{\partial z}\hat{z}, \\ \nabla\beta &= \frac{1}{r}\hat{\theta} - \nabla\gamma = -\frac{\partial\gamma}{\partial r}\hat{r} + \frac{1}{r}\hat{\theta} - \frac{\partial\gamma}{\partial z}\hat{z},\end{aligned}\tag{5.3}$$

where  $\hat{r}$ ,  $\hat{\theta}$ ,  $\hat{z}$  are unit vectors of the corresponding coordinates. So the components of the magnetic field are

$$\begin{aligned}B_r &= -\frac{1}{r}\frac{\partial\alpha}{\partial z}, \\ B_\theta &= \frac{\partial\alpha}{\partial r}\frac{\partial\gamma}{\partial z} - \frac{\partial\alpha}{\partial z}\frac{\partial\gamma}{\partial r}, \\ B_z &= \frac{1}{r}\frac{\partial\alpha}{\partial r}.\end{aligned}\tag{5.4}$$

If  $\Phi(r, z)$  is the magnetic flux embraced by the circle  $z = \text{const.}$ ,  $r = \text{const.}$ , we find that

$$\Phi(r, z) = \int_0^r B_z(r', z)2\pi r' dr = 2\pi\alpha(r, z),\tag{5.5}$$

provided that  $\alpha(0, z) = 0$ , which we may set as an appropriate boundary condition. So again, as in the rectangular model,  $\alpha$  is a measure of magnetic flux.

By choosing units appropriately, we may write the electric current from Ampère's law as

$$\vec{J} = \nabla \times \vec{B},\tag{5.6}$$

and the Lorentz force as

$$\vec{F} = \vec{J} \times \vec{B}.\tag{5.7}$$

The components of the electrical current, therefore, are

$$\begin{aligned} J_r &= (\nabla \times \vec{B})_r = -\frac{\partial B_\theta}{\partial z}, \\ J_\theta &= (\nabla \times \vec{B})_\theta = \frac{\partial B_r}{\partial z} - \frac{\partial B_z}{\partial r}, \\ J_z &= (\nabla \times \vec{B})_z = \frac{1}{r} \frac{\partial}{\partial r}(r B_\theta). \end{aligned} \quad (5.8)$$

In terms of  $\alpha$  and  $\gamma$ , equation (5.8) can be rewritten as

$$\begin{aligned} J_r &= \frac{\partial^2 \alpha}{\partial z^2} \frac{\partial \gamma}{\partial r} + \frac{\partial \alpha}{\partial z} \frac{\partial^2 \gamma}{\partial r \partial z} - \frac{\partial^2 \alpha}{\partial r \partial z} \frac{\partial \gamma}{\partial z} - \frac{\partial \alpha}{\partial r} \frac{\partial^2 \gamma}{\partial z^2}, \\ J_\theta &= -\frac{1}{r} \frac{\partial^2 \alpha}{\partial r^2} + \frac{1}{r^2} \frac{\partial \alpha}{\partial r} - \frac{1}{r} \frac{\partial^2 \alpha}{\partial z^2}, \\ J_z &= \frac{1}{r} \left( \frac{\partial \alpha}{\partial r} \frac{\partial \gamma}{\partial z} - \frac{\partial \alpha}{\partial z} \frac{\partial \gamma}{\partial r} \right) + \frac{\partial^2 \alpha}{\partial r^2} \frac{\partial \gamma}{\partial z} \\ &\quad + \frac{\partial \alpha}{\partial r} \frac{\partial^2 \gamma}{\partial r \partial z} - \frac{\partial^2 \alpha}{\partial r \partial z} \frac{\partial \gamma}{\partial r} - \frac{\partial \alpha}{\partial z} \frac{\partial^2 \gamma}{\partial r^2}. \end{aligned} \quad (5.9)$$

The components of the magnetic force are

$$\begin{aligned} F_r &= J_\theta B_z - J_z B_\theta, \\ F_\theta &= J_z B_r - J_r B_z, \\ F_z &= J_r B_\theta - J_\theta B_r. \end{aligned} \quad (5.10)$$

For the special case  $\gamma = \text{constant}$ , we find that  $B_\theta = 0$  from equation (5.4), and  $J_r = J_z = 0$  from equations (5.8) or (5.9). The Lorentz force then reduces to

$$\vec{F} = J_\theta (B_z \hat{r} - B_r \hat{z}). \quad (5.11)$$

The force-free equation therefore reduces to the current-free equation

$$J_\theta = \frac{\partial B_r}{\partial z} - \frac{\partial B_z}{\partial r} = 0. \quad (5.12)$$

By substituting expressions of the field components in equations (5.4) into equation (5.10), we obtain a single equation

$$\frac{\partial^2 \alpha}{\partial r^2} + \frac{\partial^2 \alpha}{\partial z^2} - \frac{1}{r} \frac{\partial \alpha}{\partial r} = 0, \quad (5.13)$$

which obviously is a much simpler form than that of the general force-free field equation.

Barnes and Sturrock (1972) adopted a model defined by the following boundary condition at  $z = 0$  in their calculation:

$$\begin{aligned} \alpha(r, 0) &= e^{1/2} R^{-1} r e^{-r^2/2R^2}, \\ \gamma(r, 0) &= \begin{cases} 0.5\gamma_M \cos(\pi r/2R), & r < 2R; \\ -0.5\gamma_M, & r > 2R. \end{cases} \end{aligned} \quad (5.14)$$

Since this model contains a mild singularity of the  $B_z$  component at the origin, we chose to modify the function  $\alpha(r, 0)$  slightly to avoid that singularity. The boundary conditions we have chosen for  $\alpha$  and  $\gamma$  on the plane  $z = 0$  are

$$\begin{aligned} \alpha(r, 0) &= B_0 r^2 e^{-r^2/R^2}, \\ \gamma(r, 0) &= \begin{cases} 0.5\gamma_M \cos(\pi r/2R), & 0 \leq r \leq 2R, \\ -0.5\gamma_M, & r \geq 2R, \end{cases} \end{aligned} \quad (5.15)$$

where  $\gamma(r, 0)$  has the same form as in equations (5.14). From (5.15), we obtain

$$\frac{\partial \alpha}{\partial r}(r, 0) = 2B_0 r e^{-r^2/R^2} (1 - r^2/R^2). \quad (5.16)$$

$R$  is a characteristic radius, where  $\alpha(r, 0)$  takes the maximum value  $\alpha_{max} = B_0 R^2/e$ , if  $B_0 > 0$ . In our calculation we chose  $B_0 = e/R^2$ , so  $\alpha_{max} = 1$ . Also we have  $B_z > 0$  for  $0 < r < R$ , and  $B_z < 0$  for  $r > R$  on the boundary surface

$z = 0$ . The angular displacement of foot-points of field lines, defined by  $\gamma(r, 0)$ , couple a region of positive polarity ( $r < R$ ) to a region of negative polarity ( $r > R$ ), and is proportional to  $\gamma_M$ . The maximum angular displacement for any field line is  $\gamma_M$ .

For numerical computation, it is necessary to impose boundary conditions on each of the variables  $\alpha$ ,  $\gamma$  on a closed boundary. It is convenient to choose  $\alpha = 0$  on the remaining three segments of the 'box' in which calculation are carried out, so the first field line originated from the origin point goes along the segments of the boundary, and is connected to the edge of  $r = r_{max}$ ,  $z = 0$ . This field line embraces the area of  $z > 0$ , and makes the situation similar to containing magnetic field patterns in a 'superconducting box'. The boundary values  $\gamma$  are chosen to be exponentially decreasing along the  $z$ -coordinate with a base value  $\gamma(r, 0)$  pre-set in equation (5.15). The decreasing rate is flexible to arrange. Since we are seeking for force-free field solutions with an infinite half-space boundary condition, we must adopt the size of the box sufficiently large to reduce errors due to the artificial pressure introduced by the finite numerical boundary condition. Also choosing the model (5.15) allows the magnetic field strength drop off rapidly with distance from the origin for  $r \gg R$ , so that the field configuration in the strong field region, the important part of our investigation, is therefore insensitive to the precise condition at the boundary segments.

It is of course our interest to investigate the energy argument concerning the magnetic field patterns with closed field lines and that with so-called open field



lines. Following Barnes and Sturrock (1972), we adopted the boundary condition for the open field pattern on the  $z = 0$  plane as

$$\alpha(r, 0) = \begin{cases} B_0 r^2 e^{-r^2/R^2}, & r \leq R; \\ 2 - B_0 r^2 e^{-r^2/R^2}, & r > R; \end{cases} \quad (5.17)$$

and the boundary conditions on other segments to be

$$\begin{aligned} \alpha(0, z) &= 0, \\ \alpha(r, z_{max}) &= 2.0 \left( 1 - \frac{z_{max}}{(r^2 + z_{max}^2)^{1/2}} \right), \\ \alpha(r_{max}, z) &= 2.0 \left( 1 - \frac{z}{(r_{max}^2 + z^2)^{1/2}} \right). \end{aligned} \quad (5.18)$$

It is convenient to choose the initial field configuration as

$$\begin{aligned} \alpha(r, z) &= \frac{\eta_r}{\eta_r(1 - \eta_r) + \eta_z(1 - \eta_z)} [(1 - \eta_r)(1 - \eta_z)\alpha(r, 0) + \\ &\quad \eta_z(1 - \eta_z)\alpha(L, z) + \eta_z(1 - \eta_r)\alpha(r, L)], \end{aligned} \quad (5.19)$$

where parameters  $\eta_r \equiv r/L$ ,  $\eta_z \equiv z/L$ , and we define  $L \equiv r_{max} = z_{max}$ . Equation (5.19) satisfies the boundary conditions defined in equation (5.18) and is well behaved inside the box.

However, the energy stored in the open magnetic field outside this boundary is small but not insignificant. It may be estimated, with sufficient accuracy, as the energy of the radial magnetic field (outside the boundary) of a point monopole of appropriate flux strength. The formula (Sturrock, 1985) is found to be

$$W_{out} = \frac{2\pi^2}{L} \left( 1 + \frac{\pi}{4} \right). \quad (5.20)$$

To estimate the magnetic field energy of the open-field structure, we add  $W_{out}$  to the amount calculated numerically inside the boundary.

In the two-dimensional cylindrical coordinate system, the increments of  $\alpha$ ,  $\gamma$  for the iteration scheme have the forms

$$\begin{aligned}\delta\alpha_{i,j} &= -\lambda_\alpha h_r h_z (F_r \frac{\partial\alpha}{\partial r} + F_z \frac{\partial\alpha}{\partial z}), \\ \delta\gamma_{i,j} &= -\lambda_\gamma h_r h_z (F_r \frac{\partial\gamma}{\partial r} - \frac{1}{r} F_\theta + F_z \frac{\partial\gamma}{\partial z}).\end{aligned}\tag{5.21}$$

To compute the force-free magnetic field, we set up an initial field configuration subject to the given boundary condition, and then relaxed the field lines by applying the numerical method described in Chapter 3. We calculated a sequence of magnetic field configurations for the values  $\gamma_M = 0, 0.5\pi, \pi, 1.5\pi, 2\pi, 2.5\pi$ , and  $3\pi$ , where  $\gamma_M = 0$  corresponds to the potential field. The scale sizes of the computing mesh are taken as  $L = r_{max} = z_{max} = 320$ , and the characteristic radius  $R = 14$ , so  $L \approx 23R$ . The resulting magnetic field configurations are shown in Figure 9(a)-(g). We find that field lines are pushed outwards when the maximum twisting parameter  $\gamma_M$  increases. Figure 9(h) is the corresponding open-field configuration. For this choice of size  $L$ , the results are quite acceptable for  $\gamma_M \leq 2\pi$ . However, it is obvious from the calculated field configurations that outer field lines are severely distorted by the finite boundary when  $\gamma_M$  takes larger values, for examples,  $\gamma_M = 2.5\pi, 3\pi$ .

For each case, we have computed the total magnetic field energy. The results are listed in Table 2, together with our estimate of the total magnetic energy of the corresponding open-field configuration. The relation of magnetic field energy  $W$  with the parameter  $\gamma_M$  is also shown in Figure 10.

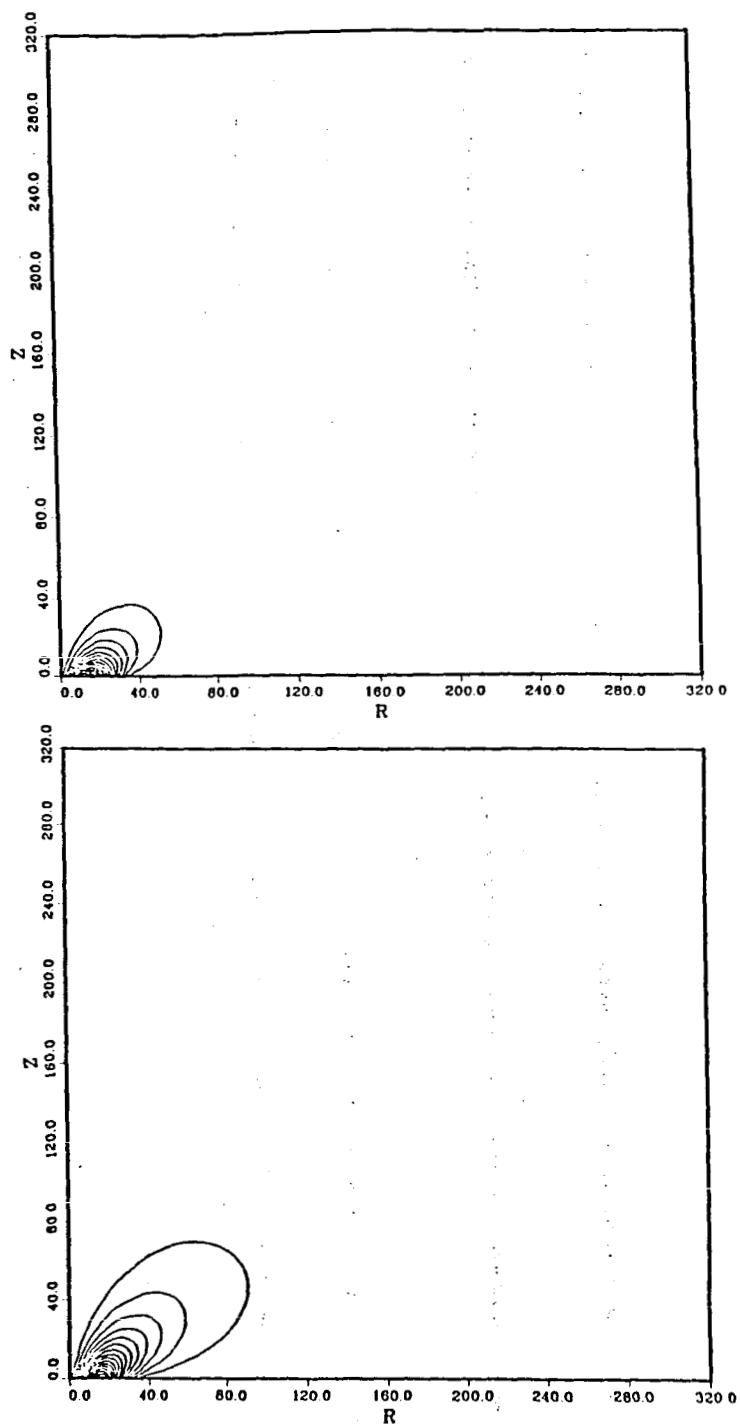
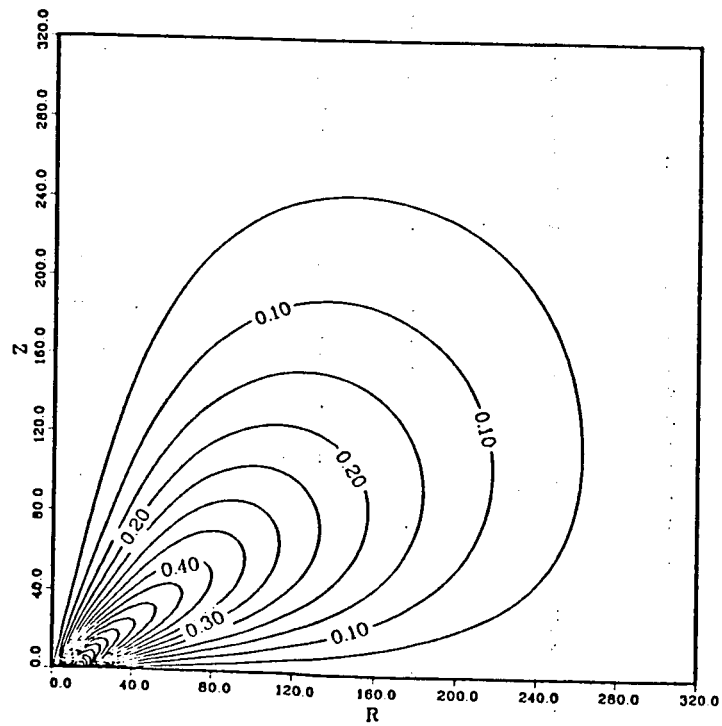
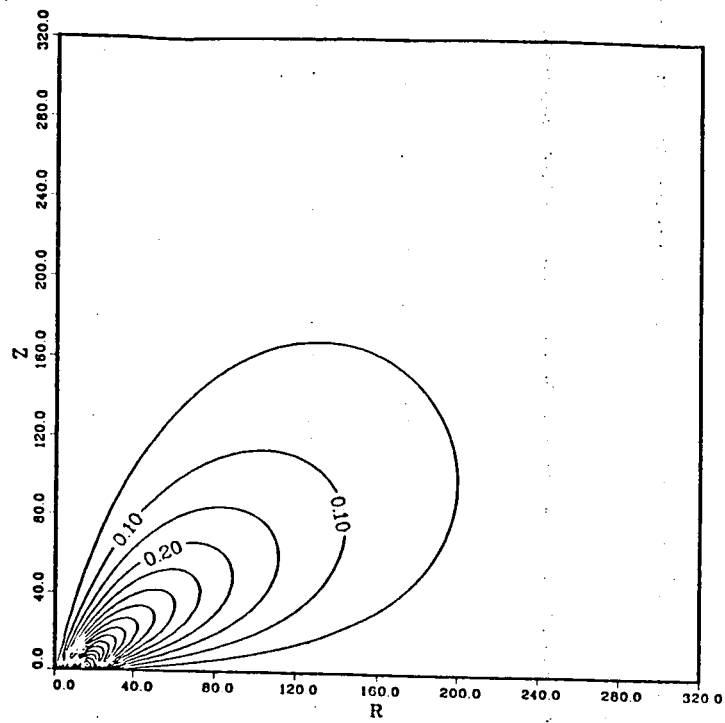
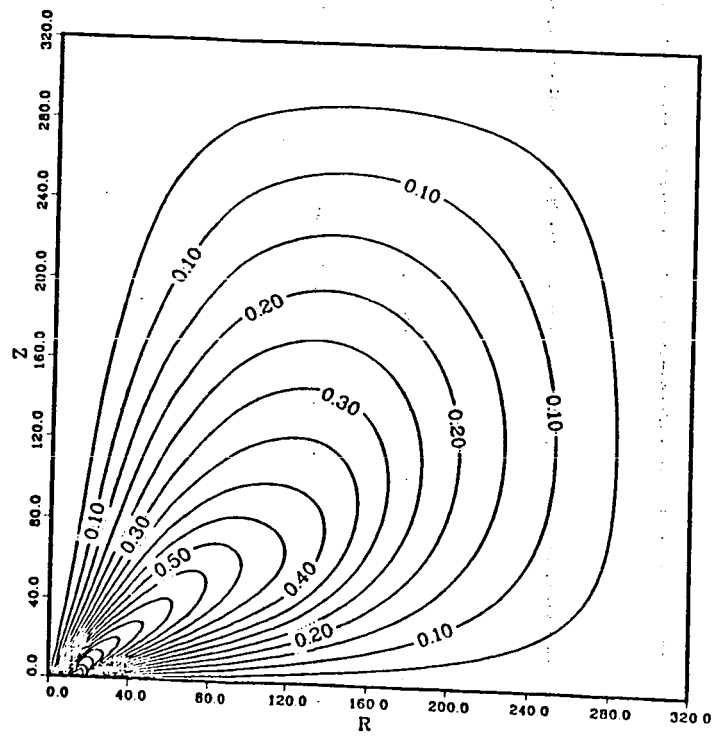
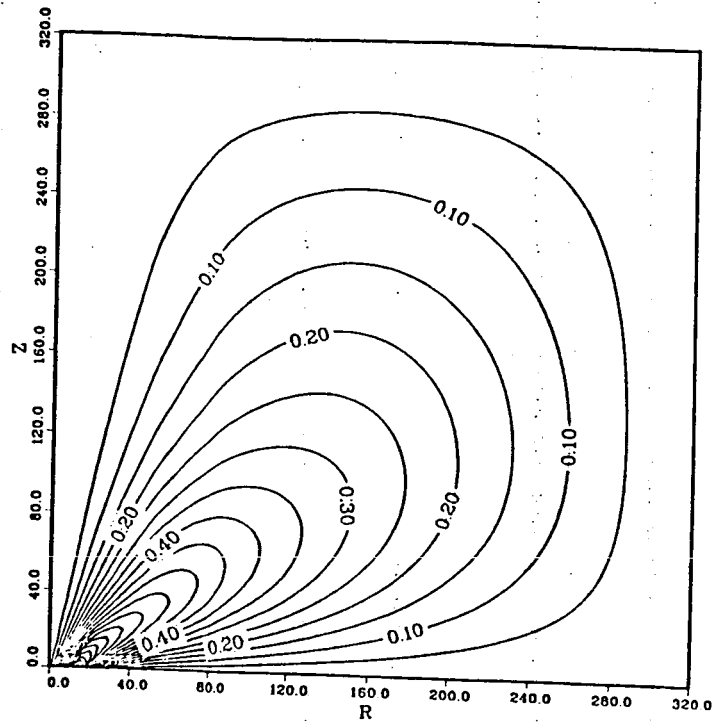


Figure 9. Contours of constant  $\alpha$  (projection of field lines on the  $r - z$  plane) for the force-free field model of cylindrical symmetry described in chapter 5, with a sequence of twisting parameter  $\gamma_M$ , the relative rotation of the regions of positive and negative polarity. Figure 9(h) gives the contour of constant  $\alpha$  for the corresponding open-field configuration.

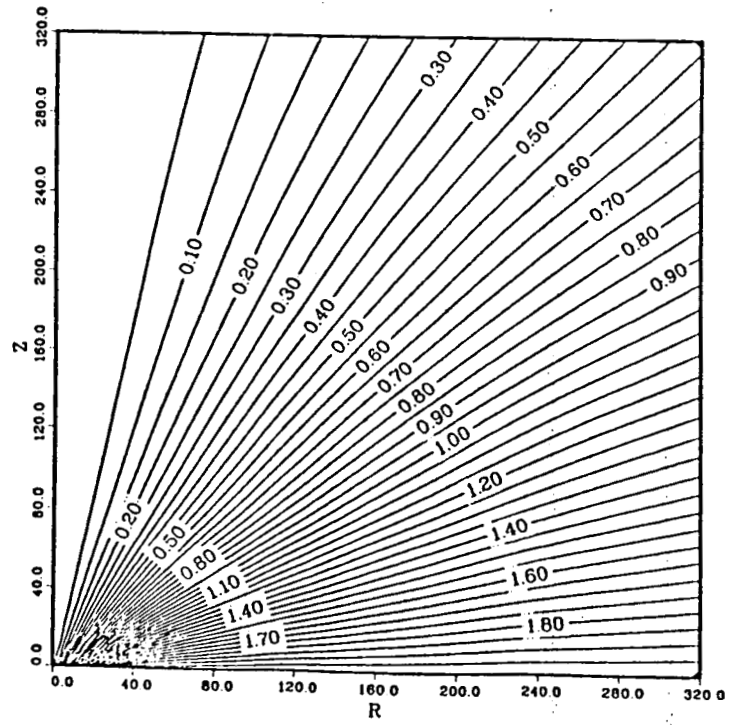
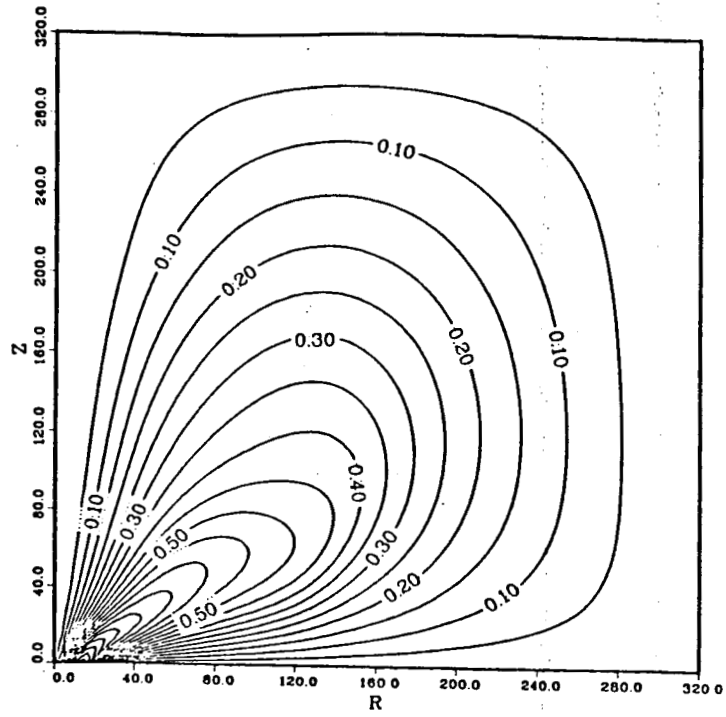
(a)  $\gamma_M = 0$ , the potential field; (b)  $\gamma_M = 0.5\pi$ .



(c)  $\gamma_M = \pi$ ; (d)  $\gamma_M = 1.5\pi$ .



(e)  $\gamma_M = 2\pi$ ; (f)  $\gamma_M = 2.5\pi$ .



(g)  $\gamma_M = 3\pi$ ; (h) the corresponding open-field configuration.

TABLE 2  
MAGNETIC FIELD ENERGY AS A  
FUNCTION OF ROTATION

$\gamma_M$	$W$
0	0.752
$0.25\pi$	0.820
$0.5\pi$	0.980
$\pi$	1.380
$1.5\pi$	1.700
$2\pi$	1.900
$2.5\pi$	2.00 <sup>a</sup>
<i>open field</i>	2.001 <sup>b</sup>

<sup>a</sup> This estimate is only approximate due to slow convergence and proximity of the boundary. However, this value estimated has been confirmed by further calculation on a mesh of size  $480 \times 480$  with application of variable grid sizes, see discussion in section 5.3. The estimate for  $\gamma_M = 3\pi$  is even less certain and is not given.

<sup>b</sup> The energy of the open field has been estimated by adding to the energy of the field within the box an estimate of the energy of the field outside the box.

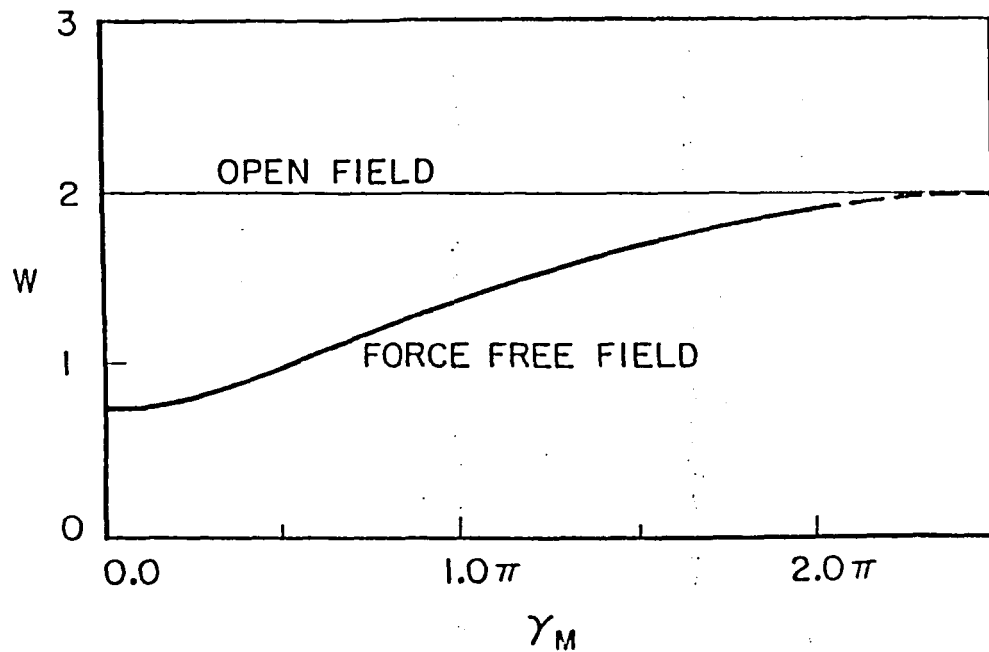


Figure 10. The magnetic field energy of the modified Barnes-Sturrock model of Chapter 5 as a function of  $\gamma_M$ , which measures the relative rotation of the positive polarity region and the negative polarity region in a cylindrically symmetric system. Also shown is the energy of the corresponding open-field configuration.



From the computed results, we see that, as the stress of the force-free field increases with the increase of the value of the parameter  $\gamma_M$ , the total magnetic field energy  $W$  approaches asymptotically, but does not appear to exceed, that of the corresponding open-field configuration. There is a striking difference between our present results and those of the earlier work by Barnes and Sturrock (1972). According to the earlier results, as seen from the  $W - \gamma_M$  curve in Figure 5 of the article by Barnes and Sturrock (1972), it appeared that  $dW/d\gamma_M > 0$ , and  $dW/d\gamma_M \approx 0.8/\pi$ , when  $\gamma_M > \pi$ ; with the increase of value of  $\gamma_M$ , the magnetic field energy  $W$  reaches the energy of the corresponding open-field configuration when  $\gamma_M \approx 1.1\pi$ , and  $W > W_{openfield}$  thereafter.

Aly (1984) has considered boundary problems of force-free fields with fixed values of the normal component  $B_n$  on the boundary surface. He has conjectured that the energy of any force-free field in a half-space domain cannot exceed that of the corresponding open-field configuration, and suggested that the results of the Barnes-Sturrock calculation were in error. It appears, therefore, that our present calculation do not support the proposal of Barnes and Sturrock (1972) that the energy of force-free field can exceed that of the corresponding open-field configuration. On the contrary, our present studies support Aly's conjecture.

### 5.3. On the Influence of Boundary

Our numerical calculation of force-free fields is carried out in a system with a closed boundary. The magnetic field then is confined inside the super-conducting box by some kind of artificial pressure produced by the finite boundary. If we

enlarge the size of the box, obviously, the magnetic field lines will follow to expand. The total magnetic field energy inside the box will increase if we reversely reduce the size of the box, because work has to be done against the magnetic field pressure to squeeze the field lines. Therefore it is expected that the estimated energy of the magnetic field contained in a finite 'super-conducting' box will exceed that of the magnetic field with an infinite external boundary.

To estimate the influence of the boundary on the calculation, we have computed the force-free field problem described in equation (5.15) of section 5.2 on boxes with different sizes. We adopted the value  $\gamma_M = 2.5\pi$ , in that case the magnetic field is expected to be largely sheared. By taking  $R = 14$ , the same as we defined in section 5.2, calculations have been performed on meshes with sizes  $r_{max} \times z_{max} = 80 \times 80, 160 \times 160$ , and  $480 \times 480$ .

The magnetic field energy (inside the box) calculated on mesh of size  $80 \times 80$  is,  $W = 1.34W_{open}$  (energy of the corresponding open-field). The field configuration of the result is plotted in Figure 11(a). One may find that the magnetic field lines are very badly distorted by comparing them with those of Figure 9(f) where calculation was done on a mesh with a scale size of  $320 \times 320$ . The magnetic field pressure on the external boundary, which we may estimate numerically, is too large to be negligible. This result has a big error from the force-free field solution of half-space domain, and therefore is not acceptable.

The magnetic field lines were more relaxed when we calculated the force-free field problem on a mesh with size  $160 \times 160$ , and the energy (inside the box)

reduced to  $W = 1.20W_{open}$ . Further we computed this force-free field model on a mesh of size  $480 \times 480$  by applying the method of variable grid sizes as described in section 3.3.(b). For convenience to compare this result with that of Figure 9(f), we plotted a section of the computed field configuration on a  $320 \times 320$  map, see Figure 11(b). It appears that the field lines expand further outward. The magnetic field energy estimated is  $W \approx W_{open}$ .

We have also computed the Barnes-Sturrock model on meshes with different scale sizes by applying our numerical method described in Chapter 3. The results tell that there are two aspects which might cause the over large field energy estimated in their calculation. The main cause is that the size of the ‘computing box’ they adopted is too small for  $\gamma_M > \pi$ . The other possible cause is that the field lines might not relax adequately to a force-free state. This point could be seen by comparing the field configurations resulting from those two different numerical approaches.

So to ensure that the results of calculation represent force-free field solutions with sufficient accuracy, it is necessary to perform the computation on meshes with large enough scale sizes to reduce the influence of the external boundary to an acceptable extent. Clearly the method of variable grid sizes has the advantage in computing large scale force-free field problems.

Another approximate method of correcting the influence of boundary is that we estimate the total magnetic field energy by the magnetic field energy inside

the box minus a correct term  $\Delta E$ .  $\Delta E$  is estimated by

$$\Delta E = \frac{1}{8\pi} \langle B_b^2 \rangle V, \quad (5.22)$$

where  $V$  is the volume of the box, and  $\langle B_b^2 \rangle$  is the average value of  $B^2$  on the boundary. In general  $\Delta E$  is a small term if the scale size of the box is chosen to be appropriately large for computation.  $\Delta E$  increases with the increase of the twisting parameter  $\gamma_M$ . For the calculation of the field model described in section 5.2, we found that  $\Delta E \leq 10^{-5} E$ , when  $\gamma_M \leq \pi$ ;  $\Delta E \sim 0.05\% E$ , when  $\gamma_M = 1.5\pi$ ;  $\Delta E \sim 0.3\% E$ , when  $\gamma_M = 2\pi$ . There are some uncertainties in these estimations, because of the difficulty of convergence of magnetic field lines in the remote weak field region. To make sure that the term expressed in equation (5.22) reflects the effect of the boundary on the total field energy of a force-free solution correctly, we need to improve our computation technique to ensure that the magnetic field lines inside the box are well converged to a force-free state ( $\vec{B} \parallel \vec{J}$ ) in the weak field region as well as in the strong field region.

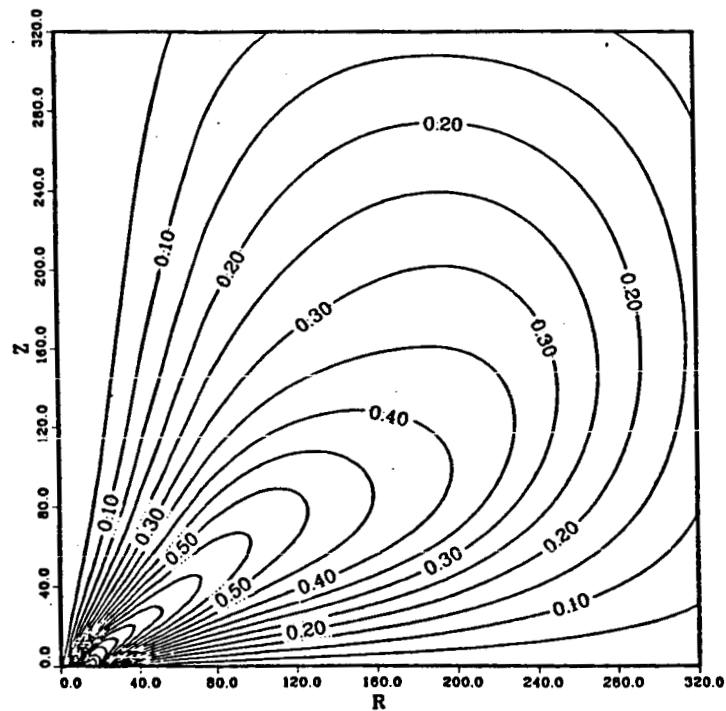
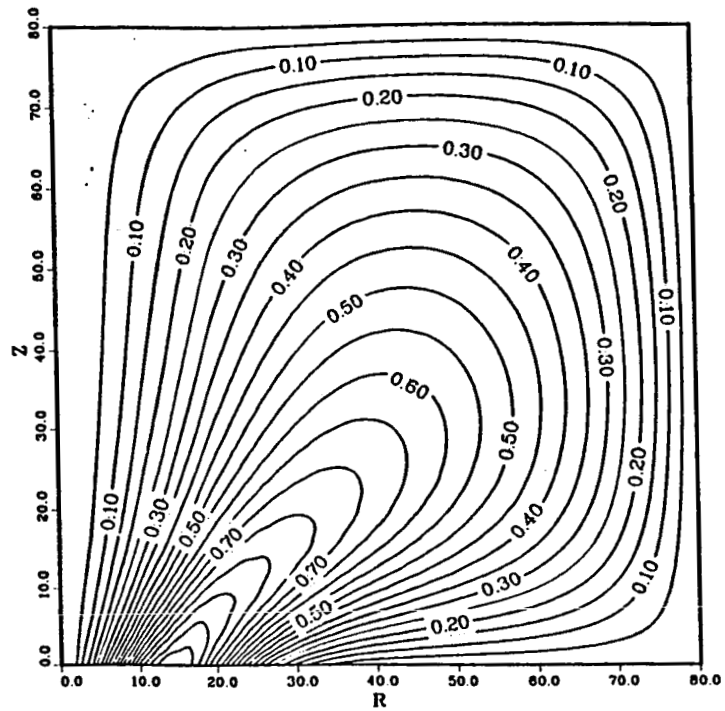


Figure 11. A comparison of magnetic field configurations of the modified Barnes-Sturrock model calculated on meshes with different scale sizes. (a) Computation performed on  $80 \times 80$  mesh. (b) Computation performed on  $480 \times 480$  mesh with variable grid sizes. Shown in this figure is a section ( $320 \times 320$ ) of the result.

## 6. ACCRETION DISK MODELS

### 6.1. Keplerian Disk Model

The accretion process of plasma captured by the gravitational force of compact objects is widely acknowledged as an important astrophysical phenomenon. This accretion process could happen in neutron stars where accreting material could be fed from interstellar medium or from the wind of a companion star in the case of binaries, which has been suggested as a model of compact  $X$ -ray sources. Black hole models for active galactic nuclei suggest that the accretion flow could be formed by falling-in matter from the body of the galaxy (gas expelled from ordinary stars via stellar winds and supernovae), or even come from intergalactic clouds captured by the galaxies (Rees, 1984). The formation of an accretion disk is a possible pattern of the accretion process. Accretion disks have been reviewed by Pringle (1981) in a general astrophysical context.

Our interest in this work is to consider the magnetic field structure and evolution of the magnetosphere of a magnetized accretion disk. We adopt the simplest hypothesis that the central compact object is being fueled steadily via a thin accretion disk. The dense plasma is contained within a thickness  $h$ , which is much smaller than the radius of the disk. Around the disk plasma may have corona-like structure. We assume that the plasma at each radius of the disk is in a nearly Keplerian orbit. The magnetic field embedded in disk plasma may be

amplified by shearing motions and possibly by turbulence-driven dynamo action. To be similar to what happens in a rotational sunspot magnetic field, a bipolar magnetic field rooted on an accretion disk may be continuously sheared due to the differential rotation, and evolve through a series of force-free configurations until some instability occurs and leads to flare-like eruption.

For simplicity, we assume that each part of the disk moves along a circular Keplerian orbit around the central object. The velocity of plasma at radius  $r$  is

$$v = \left(\frac{GM}{r}\right)^{1/2}, \quad (6.1)$$

and the angular velocity is

$$\Omega = k r^{-3/2}, \quad (6.2)$$

where  $G$  is the gravitational constant,  $M$  is the mass of the central object, and the constant  $k \equiv (GM)^{1/2}$ .

The differential rotation rate for plasma at different radii, say  $R_1$  and  $R_2$ , can be written as

$$\Delta\Omega = k(R_2^{-3/2} - R_1^{-3/2}). \quad (6.3)$$

$\Delta\Omega$  is negative when  $R_2 > R_1$ , which means that rings farther from the central object rotate at lower angular velocities. The local shearing rate, defined to estimate the shearing extent at a certain radius, is

$$S \equiv r \frac{d\Omega}{dr} = -\frac{3}{2}\Omega. \quad (6.4)$$

We assume that the strong field region of a bipolar magnetic field model remains in a region  $R_1 \leq r \leq R_2$ . At a time  $t = 0$ , the differential rotation angle

for a point at  $R_2$  relative to a corresponding point at  $R_1$  is  $\Delta\varphi = 0$ ; then at time  $t$ , from equation (6.3), we may find

$$\gamma_M \equiv |\Delta\varphi(R_2, t)| = |\Delta\Omega|t, \quad (6.5)$$

so we may write

$$\Delta\varphi(r, t) = -\frac{\gamma_M}{(R_1^{-3/2} - R_2^{-3/2})}(R_1^{-3/2} - r^{-3/2}), \quad (6.6)$$

which indicates the twisting angle at radius  $r$  of the disk relative to a corresponding point at  $R_1$ . Figure 12 shows the differential rotation of a circular Keplerian disk at times  $t = t_0, t_1, t_2, t_3, t_4$ , with corresponding values  $\gamma_M = 0, \pi/2, \pi, 3\pi/2, 2\pi$ . In the calculation, we adopted  $R_1 = 1.0$ ,  $R_2 = 3.0$ .

## 6.2. Force-Free Field Models and Calculation

In this section we are going to investigate the evolution of force-free fields with footpoints fixed on a Keplerian accretion disk. As we discussed in section 5.2, for the cylindrically symmetric situation the flux distribution of magnetic field could be described by the boundary value of one of the Clebsch variables, i.e.  $\alpha(r, 0)$ . The numerical method we discussed in the previous chapters is convenient for us to compute force-free field models by adopting various kinds of distribution of  $\alpha(r, 0)$  on the accretion disk. The twisting extent of the magnetic field due to the differential rotation of the disk can be described by the function  $\gamma(r, 0)$ , which may simply have the form of (6.6).



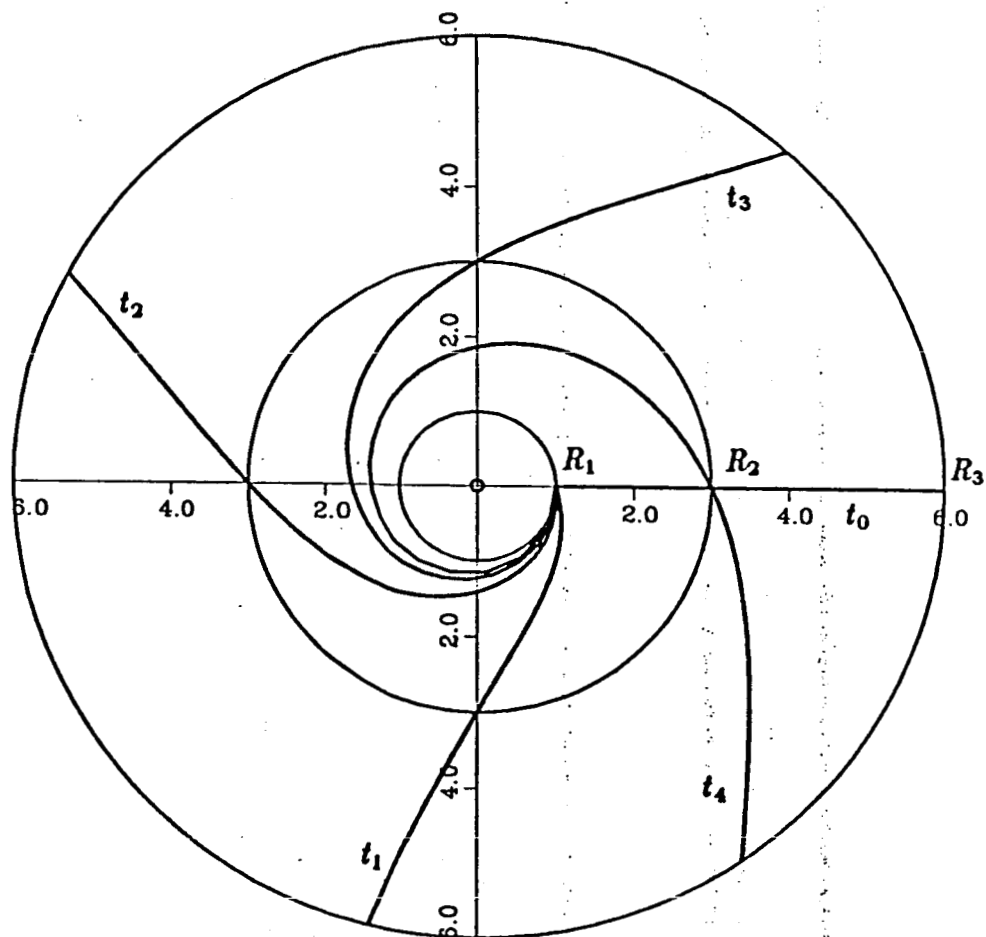


**Figure 12.** Illustration of the differential rotation of a Keplerian accretion disk.

(a) Single Field Model

For a simple case we choose the boundary condition of the Clebsch variables on the disk as

$$\alpha(r, 0) = \begin{cases} 0, & 0 \leq r < R_1; \\ B_0(r - R_1)^2 e^{-(r-R_1)^2/R^2}, & r \geq R_1; \end{cases} \quad (6.7)$$

and

$$\gamma(r, 0) = \begin{cases} 0, & 0 \leq r < R_1; \\ -\frac{\gamma_M}{(R_1^{-3/2} - R_2^{-3/2})} (R_1^{-3/2} - r^{-3/2}), & r \geq R_1; \end{cases} \quad (6.8)$$

respectively, where  $\gamma_M$  defines the shearing angle between corresponding footpoints at  $R_1$  and  $R_2$ .  $\alpha(r, 0)$  has a form similar to the rotational sunspot model adopted in equation (5.15) except that we shift the footpoints of field lines a distance  $R_1$  in the radial direction. It is easy to find that  $\alpha(r, 0)$  reaches its maximum value at  $r = R_1 + R$ , so the magnetic field changes its polarities at this radius. We start our calculation by taking  $\gamma_M = 0$ , which gives the corresponding potential field configuration. Then we increase the value of  $\gamma_M$  step by step, which indicates the continuous twisting of the field during the differential rotation of the disk. In our calculation we adopted  $B_0 = e/R^2$ ,  $R = 16.0$ ,  $R_1 = 16.0$ , and  $R_2 = 48.0$ , so we have  $0 \leq \alpha(r, 0) \leq 1$ . The magnetic field configurations for  $\gamma_M = 0$ , and  $2\pi$  are shown in Figure 13(a), (b), respectively. The computation was performed in a box of a scale size of  $400 \times 400$ , where we took larger grid sizes when  $r, z > 320$ .

The results of this calculation, as expected, indicate that the magnetic field lines expand towards the corresponding open-field configuration during the rotation of the accretion disk.

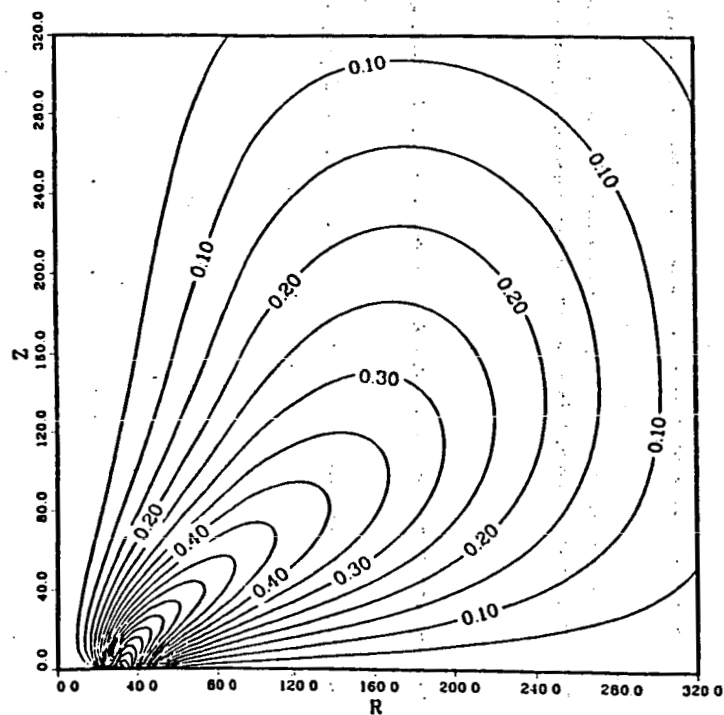
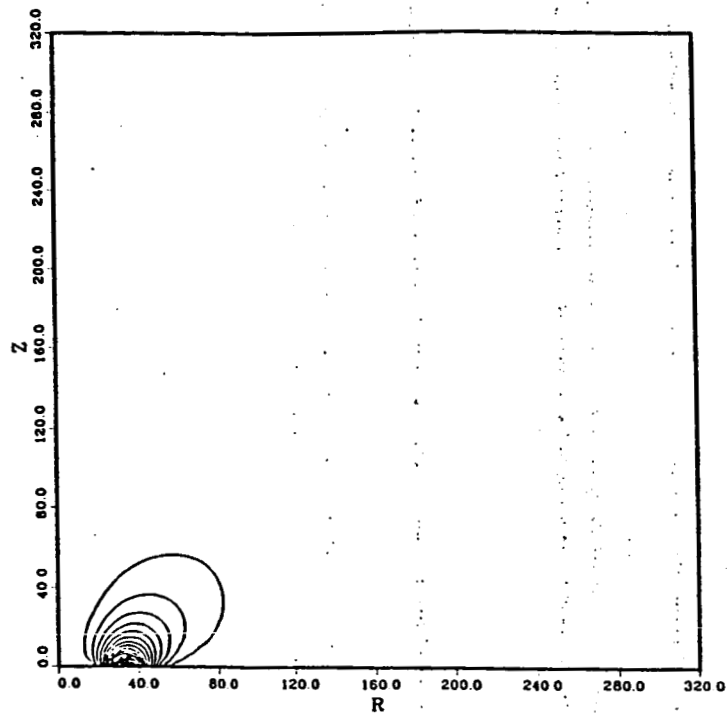


**Figure 13.** Contours of constant  $\alpha$  for a single force-free field model of a Keplerian accretion disk. The differential rotation angle between  $R_1 = 16.0$  and  $R_2 = 48.0$  is defined by  $\gamma_M$ . (a)  $\gamma_M = 0$ , potential field; (b)  $\gamma_M = 2\pi$ .

(b) Calculation of Magnetic Torque

From the conservation of angular momentum (Jackson, 1962),

$$\frac{d}{dt} \int_V L d^3x + \int_V \nabla \cdot \mathbf{M} d^3x = 0, \quad (6.9)$$

the total magnetic torque can be calculated by a surface integral

$$\vec{Q} = - \int_S \vec{n} \cdot \mathbf{M} dS, \quad (6.10)$$

where  $L$  is the angular momentum density,  $\vec{n}$  is the normal unit vector of the boundary surface  $S$ , and the flux of angular momentum  $\mathbf{M}$  is the tensor defined by

$$\mathbf{M} = \mathbf{T} \times \vec{r}, \quad (6.11)$$

where  $\mathbf{T}$  is the Maxwell stress tensor shown in equation (2.5).

For our accretion disk field model, the magnetic torque can be estimated by a surface integral on the disk plane. Therefore equation (6.10) reduces to

$$\vec{Q} = - \int_a \hat{z} \cdot \mathbf{M} da, \quad (6.12)$$

where  $da$  is the element of area on the plane of the disk.

In the situation we consider, there are no electric field terms attributing to the Maxwell stress tensor. We substitute the expression of  $\mathbf{T}$  in equation (2.5) into equation (6.11), obtain an expression for angular momentum flux  $\mathbf{M}$ , and then substitute this into equation (6.12). We then obtain

$$\vec{Q} = \frac{1}{4\pi} \hat{z} \int_a r B_z B_\theta da + \frac{1}{8\pi} \hat{\theta} \int_a r B^2 da. \quad (6.13)$$

The second term is due to the magnetic field pressure on the disk, and has a tendency to bend the disk plane. The first term is what interests us in this calculation, and is due to the tension along the field lines. We may rewrite this term in the form

$$Q_z = \frac{1}{2} \int r^2 B_z B_\theta dr. \quad (6.14)$$

For the cylindrically symmetric case, the azimuthal component of the magnetic force can be derived by substituting equation (5.5) into equation (5.10). We find that

$$F_\theta = \frac{1}{r} B_r \frac{\partial}{\partial r} (r B_\theta) + B_z \frac{\partial}{\partial z} B_\theta, \quad (6.15)$$

which can be rewritten as

$$F_\theta = \frac{1}{r} \nabla (r B_\theta) \cdot \vec{B}. \quad (6.16)$$

If the magnetic field is force-free,  $F_\theta$  is zero everywhere. This indicates that  $r B_\theta = \text{constant}$  along the magnetic field line. From the conservation of the magnetic flux, we know that  $\vec{B} \cdot d\vec{a} = \text{constant}$  along a magnetic field flux tube. So for our bipolar force-free magnetic field model, the integral in equation (6.14) vanishes, i.e.  $Q_z = 0$ . Hence if  $R_{rv}$  is the 'reversing radius' of the polarity of the bipolar magnetic field, the following condition must be fulfilled :

$$Q_1 = -Q_2, \quad (6.17)$$

where

$$Q_1 = \frac{1}{2} \int_{R_0}^{R_{rv}} r^2 B_z B_\theta dr,$$

$$Q_2 = \frac{1}{2} \int_{R_{\text{in}}}^R r^2 B_z B_\theta dr.$$

We have computed the magnetic field energy  $W$ , and magnetic torques  $Q_1$ ,  $Q_2$ , and  $\Delta Q$  for a series of values of  $\gamma_M$  in the model described in section (a). For  $\gamma_M = 2\pi$ , as an example of our calculation, we find that

$$Q_1 = -1.000 \times 10^{-2},$$

$$Q_2 = 1.000 \times 10^{-2},$$

$$\Delta Q \equiv Q_1 + Q_2 = 4.572 \times 10^{-6} \approx 0,$$

so that the difference between the computed  $|Q_1|$  and  $|Q_2|$  is within 0.05%.

The curves relating  $W$  to  $\gamma_M$  and  $Q$  to  $\gamma_M$  ( $Q \equiv |Q_1| = |Q_2|$ ) are plotted in Figure 14.

From the results of the calculation, one may see that the magnetic energy  $W$  increases from the minimum level of a corresponding potential-field state, and approaches asymptotically towards the open field energy. This result is in agreement with what we obtained in Chapter 5. From the energy theorem, the increase of the magnetic field energy is the result of work done against the azimuthal force,  $F_\theta$ , during the twisting of the field lines. When  $\gamma_M$  is large enough, the magnetic field energy is close to the open field energy and nearly saturated. Any further twisting of the field will not pump significantly more energy into the magnetosphere of the accretion disk. The torque  $Q$ , therefore, increases from zero to its maximum value, and then decreases and approaches zero with further increase of the twisting amount  $\gamma_M$ . Our calculation shows

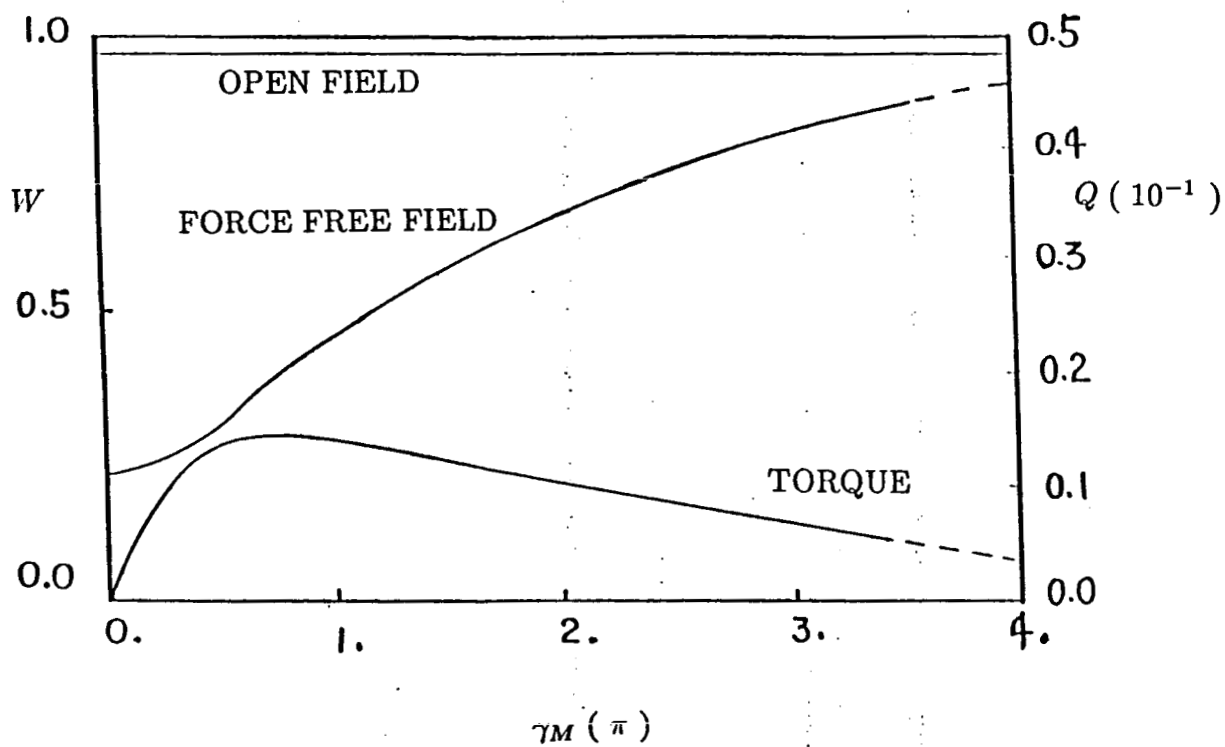


Figure 14. The magnetic field energy  $W$  and magnetic torque  $q$  of a single field model of a Keplerian accretion disk as functions of  $\gamma_M$ .

that the turning point for  $W$  ( where  $\frac{\partial W}{\partial \gamma_M}$  takes maximum value) and hence for  $Q$ , occur at the value of  $\gamma_M$  of about  $0.7\pi$ .

The magnetic torque obviously contributes to the viscosity of the disk plasma.

### (c) Multi-field Models

The magnetic field of an accretion disk may have complex structures. As a further application of our numerical method, we have computed force-free field models with more than one bipolar magnetic field co-existing on a single accretion disk. The purpose of this calculation is to investigate the mutual influence of those magnetic fields during the evolution process. The numerical method applied in the calculation will lead to field configurations in their minimum energy states, although the physical process leading to the results will not be shown in the iteration process.

For two adjacent bipolar magnetic fields on an accretion disk, the evolution of the fields depends on the distribution of the polarities of the fields. If two magnetic fields have opposite polarities in their neighboring zone, reconnection of the magnetic field lines may happen, and could play an important role in deciding the field configuration. This situation has some similarity with Sweet's solar flare model (Sweet 1958). The expansion of field lines due to twisting of the footpoints may enhance this reconnection process.

Another case is that the two bipolar magnetic fields have the same polarity



in their neighboring zone. Then reconnection of field lines will not occur in this region. The general field configuration depends on the balance of the magnetic pressure of the two fields.

To study field evolution in this case, we adopt a model described by the following boundary conditions

$$\alpha(r, 0) = \begin{cases} 0, & 0 \leq r < R_1; \\ \text{Sin}\left(\frac{r-R_1}{2R}\pi\right), & R_1 \leq r \leq R_1 + 2R; \\ \text{Sin}\left(\frac{r-R_1}{2R}\pi\right), & R_1 + 2R \leq r \leq R_2; \\ 0, & r > R_2; \end{cases} \quad (6.18)$$

where  $R_2 \equiv R_1 + 4R$ . And  $\gamma(r, 0)$  chosen has the same form as that of expression (6.8). With this choice, there are two bipolar magnetic fields embedded on the disk. One is rooted in  $R_1 < r < R_1 + 2R$ , and the another in  $R_1 + 2R < r < R_2$ . In the calculation we choose  $R = 16.0$ , and  $R_1 = 16.0$ .

The magnetic field configurations for  $\gamma_M = 0, \pi, 2\pi$ , and  $3\pi$  are plotted in figure 15 (a), (b), (c), (d) respectively, where  $\gamma_M$  is defined in equation (6.5).

Figure 15 (a) represents the current-free field configuration, so the azimuthal component of the magnetic field equals zero everywhere. This field configuration gives the minimum magnetic energy with the given boundary value of  $\alpha(r, 0)$ , or  $B_z(r, 0)$ . The parameter  $\gamma_M$  is a measure of the extent of the twisting of the magnetic field. The local shearing rate, defined in equation (6.4), is proportional to  $r^{-3/2}$ . The differential rotation, therefore, is larger for the inner field, so the inner field will be twisted more than the outer field during the differential rotation. Hence in the initial stage the inner field expands with higher magnetic pressure. The outer field is pressed downwards, and even overlaid by the inner

field (see Figure 15 (b), (c)). However, during the later evolution period, the situation might be reversed. As we know from the study of the single field model, the inner field (energy) is nearly saturated after a certain extent of twisting, so that field pressure does not increase further with the differential rotation of the accretion disk, but the outer field can still be greatly enhanced. It is now its turn to expand and press the inner field inwards. An example of the field configuration for this later situation is shown in Figure 15 (d). If there is no instability occurring, we expect that both fields will extend towards a combined open-field configuration.

This field model has obviously been idealized. We have assumed that all the fields have cylindrically symmetric structures, but the calculation show us qualitatively the possible effects of the mutual interaction of neighboring magnetic fields on their evolution due to the differential rotation.

### 6.3. Extra-Galactic Radio Sources and the Accretion-Disk Flare Model

The discrete sources of radio emission were first distinguished from the general background radiation during the 1940's, and initially were thought as galactic radio stars (Kellermann, 1974). Later identification made it clear that at least some of the discrete sources were of extra-galactic origin. Galaxies which are identified with strong radio sources are generally referred to as 'radio galaxies'. Another class of radio sources is usually referred to as 'quasi-stellar radio sources', or radio emitting quasi-stellar objects (QSO's) or 'quasars', where the

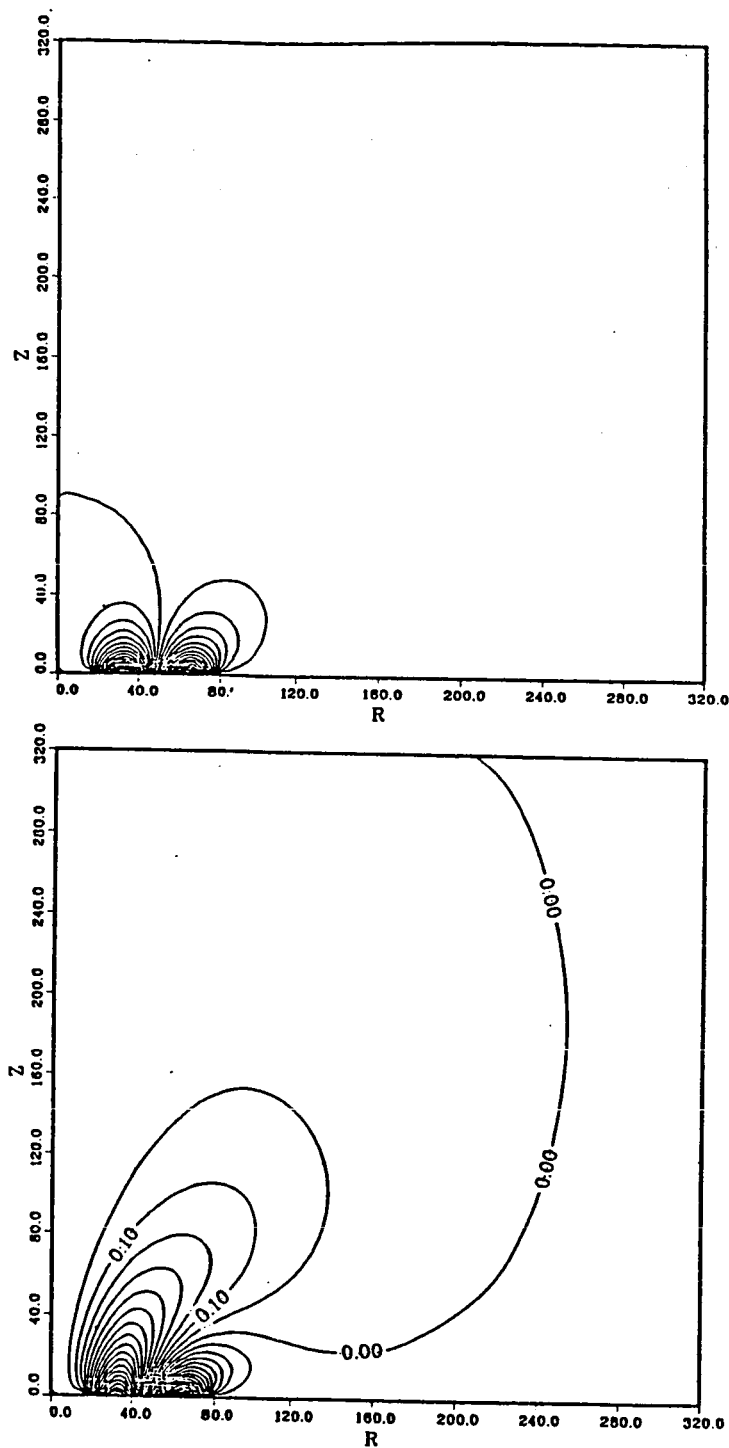
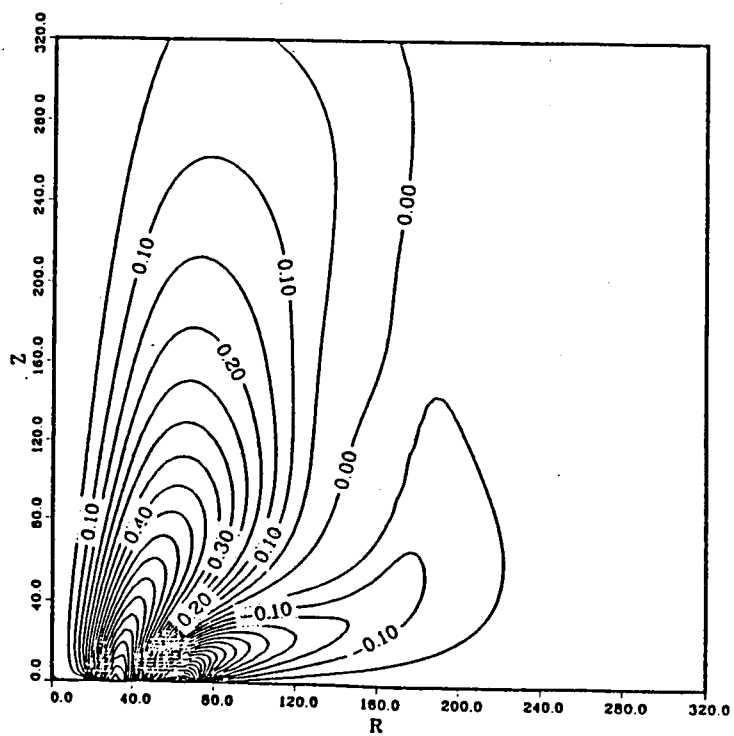
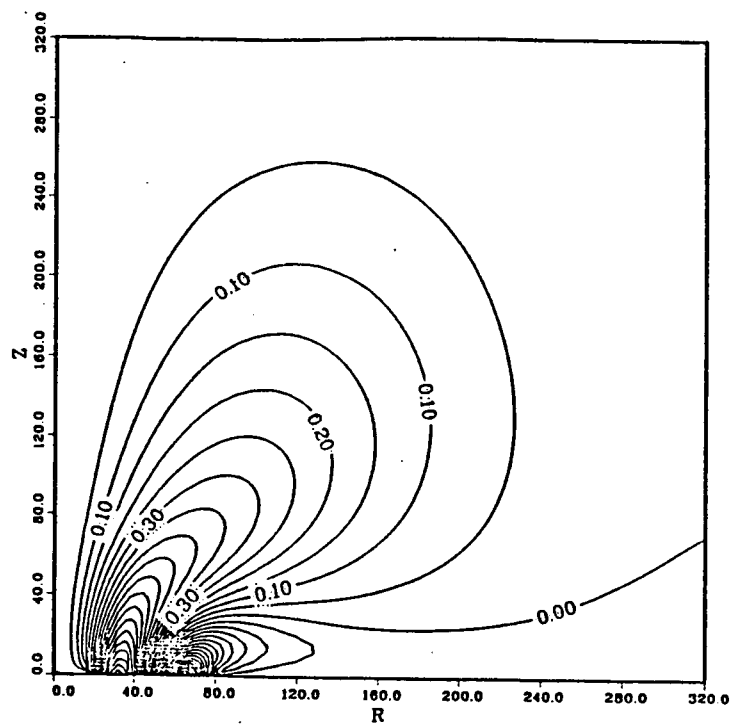


Figure 15. Contours of constant  $\alpha$  for a double field model of an accretion disk. The differential rotation angle between  $R_1 = 16.0$  and  $R_2 = 80.0$  is defined by  $\gamma_M$ . (a)  $\gamma_M = 0$ ; (b)  $\gamma_M = \pi$ ;



(c)  $\gamma_M = 2\pi$ ; (d)  $\gamma_M = 3\pi$ .

word 'quasar' is generally used to refer to the entire class of stellar-type objects with large apparent red shifts.

The total power radiated at radio frequencies extends from about  $10^{38} \text{ erg/s}$  from so-called normal galaxies, to  $10^{41} \text{ erg/s}$  from the weaker radio-emitting elliptical galaxies such as M87, and up to  $10^{45} \text{ erg/s}$  for the most luminous radio galaxies such as Cygnus A and 3C295 and many quasars. It is generally accepted that the radio emission from both galaxies (including our own Galaxy) and quasars is due to synchrotron emission from relativistic particles moving in magnetic fields. The amount of energy require in the form of relativistic particle is, however, very great, and the source of energy and its conversion into relativistic particles has been one of the outstanding problems of modern astrophysics.

Observation indicates that for most of the sources a simple single-component structure is very rare. Often the source is extended along a single axis, and the most common configuration is the double structure where most of the emission comes from two well-separated components. Frequently the two components are quite surprisingly of approximately equal size, as for example shown by the map of Cygnus A shown in Figure 16 (Mitton and Ryle, 1969).

New aperture-synthesis arrays (Davis et.al. 1980) and new image-processing techniques (Cornwell and Wilkinson 1981) have allowed radio imaging at sub-arcsecond resolution with high sensitivity and high dynamic range; as a result, the complexity of the brighter sources has been revealed clearly for the first time. Many contain radio jets, i.e. narrow radio feature between compact cen-

tral 'cores' and the more extended 'lobe' emission. Figure 17 shows the VLA maps of the jets in the weak radio galaxy M84 at 4.9 GHz (Bridle and Perley 1984). The formation of extra-galactic radio jets is one of the most challenging problems of modern astrophysics.

As an early effort to explore the physical nature of the extra-galactic radio sources, Sturrock and Barnes (1972) proposed a mechanism, called 'galactic flares'. They suggested that the magnetic field linking the inner and outer part of a disk may be distorted along a sequence of force-free configurations and lead to an open-field configuration. They conjectured that the transition from the closed configuration to an open configuration will be effected by an MHD 'eruptive' instability. The magnetic free energy may then be released explosively by the flare mechanism. The radio clouds ejected from galaxies and quasars then form the extra-galactic radio sources. However, one shortcoming of this model is that the conjecture was based on the result of their earlier calculation about the magnetic field energy of closed configuration and of corresponding open configuration (Barnes and Sturrock 1972), which has now been found to be incorrect (see Chapter 5).

In a recent article, Sturrock (1985) proposed a flux-tube model. He suggested that the flux tube is rooted in an accretion disk, then differential rotation of the disk may lead to a progressive stretching of the loop, and finally lead to ejection of the plasmoid comprising a toroid.

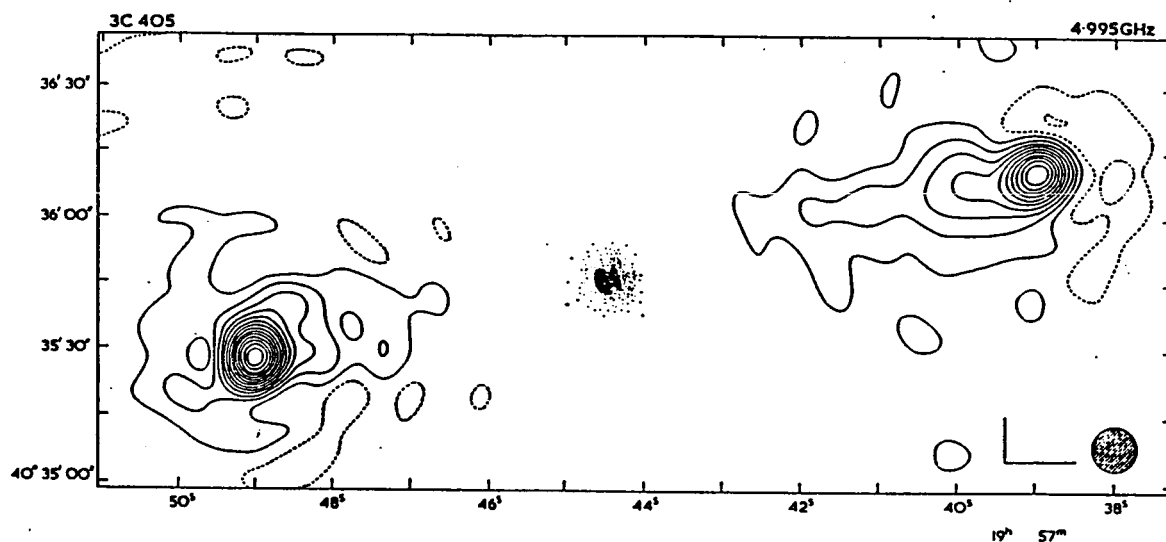


Figure 16. *Brightness distribution of the intense radio galaxy Cygnus A at 6 cm observed with the 6-second-of arc beam of the Cambridge 1-mile aperture synthesis radio-telescope (taken from Mitton and Ryle, 1969).*

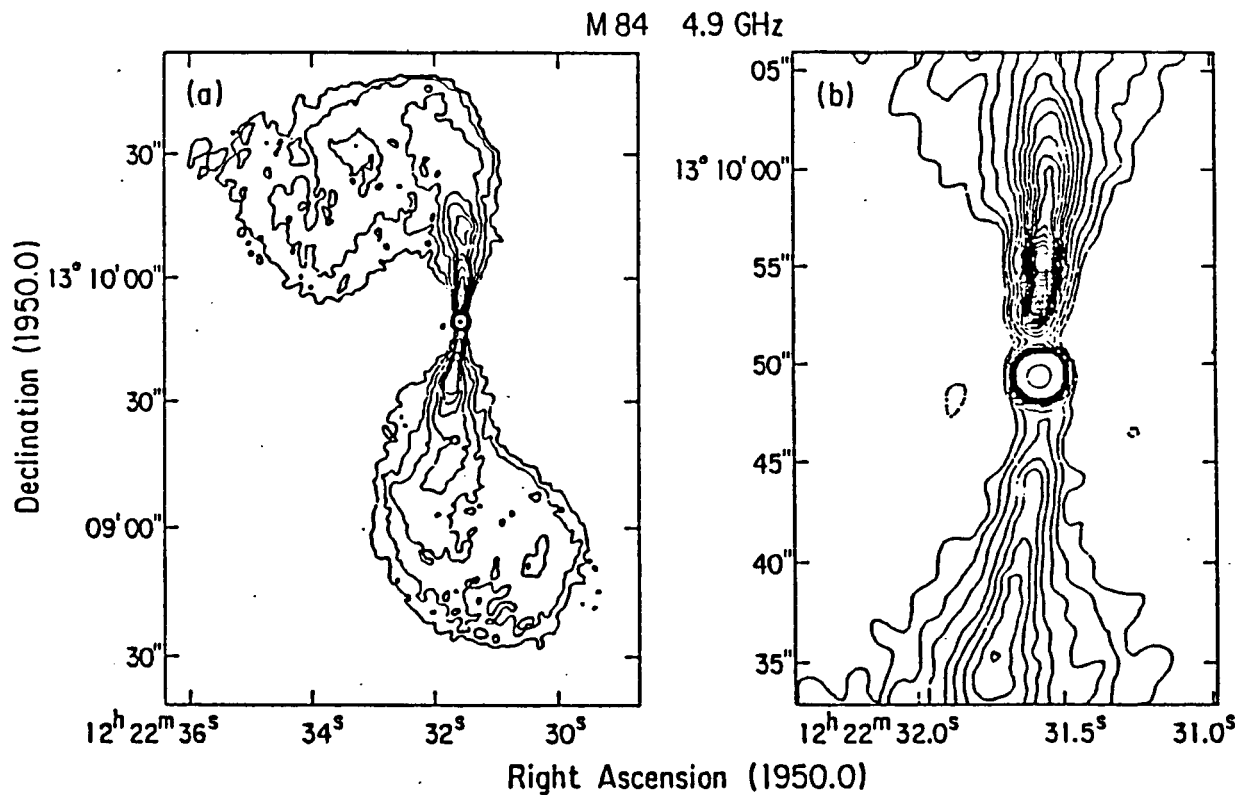


Figure 17. VLA maps of the jets in the radio galaxy M84 at 4.9 GHz, with the right panel showing detail of the central region. The peak on these maps is the radio core. Note the one-sided bright base of the northern jet and the faint cocoon of emission flaring from both jets beyond 5" from the core (taken from Bridle and Perley, 1984).



The calculation of models in section 6.2 (a), (b) and (c) is a numerical effort to investigate the so-called 'accretion disk flare' model for producing extragalactic radio sources. The calculation of the single field model in section 6.2 (a) shows that the magnetic field rooted on an accretion disk could be distorted by the strong differential rotation of the accretion disk, and evolve from an initially current-free state through a series of force-free state towards an open-field state. This process is similar to what could happen for a rotating sunspot. One may expect flare-like activity to occur in the magnetosphere of the disk. The magnetic field lines may be reconnected through the tearing-mode instability. The ejected plasmoid may have a toroidal magnetic-field configuration because of the reconnection. It is not clear yet that whether a fast reconnection will occur when the field is highly stressed but still closed or after it reaches the open-field state.

Since the magnetic field configuration may have a statistically symmetric distribution with respect to the disk plane, radio clouds may be produced at the same time or different times and ejected in opposite directions.

The calculation of the double field model in section 6.2.(c) is to investigate the somewhat more complicated and also more important situations where more than one bipolar field co-exist on the accretion disk. With the strong differential rotation of the disk, the inner field will be highly stressed, by the meantime, the outer field will be highly pressed by the inner field. A typical field configuration for this situation is shown in Figure 15 (c). The important point is where the

instability might take place first. From the changes of the field configuration with the rotation of the disk, it seems that reconnection could happen first either in the inner field or in the outer field, which may depend on the distribution of their magnetic fluxes. Obviously, the expansion of the outer field might trigger the explosion of the already highly stressed inner field, then the outer field enters an explosive phase itself. The plasma cloud produced by the first eruption could be accelerated outwards by the successive explosion. If the highly pressed outer field has stored field energy more than its corresponding open-field energy, it may expand to an open-field configuration. A series of islands of magnetized plasma may be formed during the explosively expanding process. Since the direction of the explosion is outwards, a pair of jet-like radio clouds may be produced.

It also seems possible that the instability and reconnection may occur first in the outer field region. The Figure 15 (c) shows that a magnetic-tail-like structure is formed in the outer field region. The pressure from the inner field may produce intense current density in this region. Such a situation is susceptible to magnetic field reconnection by the tearing-mode instability.

The mutual interaction between the neighboring fields seems to increase the possibility of instability. Any instability occurring in one field may lead to a series of instabilities, eruptions, and mass ejections. We propose that such a mechanism is a candidate for producing extra-galactic radio jets. Further study of this mechanism is under way.

## 7. DISCUSSION

### 7.1. On the Numerical Method

From the calculation of two-dimensional force-free magnetic field configurations, the numerical method presented in the previous chapters is simple in concept, fairly simple in formulation and operation, and appears to offer a promising approach for the calculation of general force-free magnetic field configurations.

In the early stage, calculations were performed on uniform meshes, on which grids have the same size. We have found that there is a great advantage in applying a multigrid method in computing force-free magnetic field problems subject to given boundary conditions. Generally we start our calculation on an initial field configuration, of which the boundary values of Clebsch variables are specialized for the astrophysical model concerned. Obviously the initial field configuration so defined could be very different from the final force-free field solution. As the first step in the multigrid method, the computation is performed on a coarse mesh. This offers a rapid convergence of the field configuration towards the force-free state. To obtain higher accuracy, further computations are performed on a finer mesh, starting from the field configuration derived from the coarse mesh computation by interpolation.

A shortcoming of computing on a uniform mesh is that when the field is highly stressed one must calculate the field structure over a very large region, due to the tendency of the force-free field to inflate, moving towards an open-field

configuration. To diminish the influence of the external boundaries, one has to perform computation on a mesh of large scale size so containing a large number of grids. As indicated by the alignment of the current with the field lines, we find that the convergence of the field towards the force-free field configuration in the weak field region is usually much slower than that in the strong field region if we adopt a uniform mesh. This usually requires quite long computing time in a VAX/750 to obtain results with satisfactory accuracy. To improve our computer program, we have adopted the adaptive-grid technique, which we have discussed in Chapter 3. By this technique, computation is carried out on a numerical mesh with variable grid sizes. The grid size is small in the strong-field region and large in the weak-field region. So the total grid number needed for the computation will be reduced, and the situation of dealing with difficulty of convergence in the weak field region will be improved.

Experience from practice tells that the most efficient way so far in computing large scale force-free magnetic fields is to combine the multigrid method and the adaptive-grid technique.

To simulate real astrophysical magnetic-field configurations, calculation must be executed in three-dimensions rather than only two-dimensions as done in this work. The experience gained from  $2-D$  calculation, and techniques such as the multigrid and adaptive-grid methods, would be very useful for the  $3-D$  calculations. The success in the  $2-D$  computation makes us feel confident that the extension of the computer program into a  $3-D$  code will be straightforward.

However, 3 - D calculations will require a more powerful computer than the VAX/750 that was used for the present calculations.

We have been also considering other possible developments in numerical techniques, which are based on our present work. One is to include the gradient of the plasma pressure, to extend the numerical program into a code for computing general magnetohydrostatic equilibria. Another consideration is to let the field evolve in time, so as to obtain a method of simulating the dynamic evolution of a magnetized plasma. As the first step in exploring the possibility of these approaches, we need to rewrite the MHD equations in forms expressing the magnetic field  $\vec{B}$  in terms of the Clebsch variables  $\alpha$  and  $\beta$ . Such a representation has been discussed elsewhere ( Birn and Schindler, 1981 ).

## 7.2. On the Astrophysical Applications

There are two types of problems for which one needs the capability of computing force-free fields. One of these is the calculation of the field patterns that will be produced by certain models of astrophysical systems. Our calculation and discussion of the magnetic fields of a rotational sunspot and Keplerian accretion disks are examples of such a kind of problem. For this category of problems, the specification of the field in terms of the boundary conditions of the Clebsch variables is appropriate and convenient.

For the cases described, the total magnetic field flux is constant when one of the Clebsch variables, say  $\alpha$ , is fixed on the boundary. The evolution of

the magnetic field structures due to twisting or shearing of the footpoints can be studied by calculation of the force-free fields with the boundary conditions given by fixed values of  $\alpha$  and a series of values of another Clebsch variable  $\beta$  (or  $\gamma$ ). The study of magnetic field configurations by this method will give us informations about the increase of total field energy, the current-field structure, and the formation of a current-sheet during the twisting or shearing process. As a further application of the method, we may study the evolution of magnetic fields with the same total flux and under the same situation of twisting or shearing but having different distribution of magnetic flux on the photosphere. The purpose of this study is to investigate what kinds of field distributions are likely to lead to flare occurrences.

The study of the magnetic field structure of a rotating sunspot has indicated that the force-free field energy approaches asymptotically the open-field energy but does not exceed it. The calculation of the magnetic torque in Chapter 6 gives further support to this result. A question then arises naturally concerning current flare theories. For the occurrence of a solar flare due to the rotation of a sunspot, how could the magnetic field configuration go through an open-field stage, then release field energy through reconnection? Alternately, is there a physical process that may lead the energy stored in the magnetic field with closed field lines to exceed the energy of a corresponding open-field?

As indicated by Priest (1981), flares may be caused by the instabilities of certain magnetic field configurations, and the reconnection of field lines could

start when the magnetic field has in general a configuration with closed field lines. The most probable type of instability responsible for flare occurrences is known as the 'tearing mode' resistive instability. It is obviously a key question to solar physicists to determine at what point the force-free field assumption breaks down and this dynamic process should be included, when continuing to twist a flux tube, or to shear a magnetic arcade.

Three-dimensional study of force-free magnetic field configurations will help us in understanding some aspects of these challenging problems in flare theory. For example, we may calculate the three-dimensional space distribution of current, and determine the local enhancement of currents with the evolution of the field configuration. By this method, we may also study the evolution of complex magnetic field structures, and the mutual interaction among neighboring magnetic fields in the active region of the sun, or other astrophysical objects. However, to find the final solutions to those problems, it seems that we need far more comprehensive studies, including MHD simulations and the plasma simulations, together with theoretical analysis.

Another class of problem which needs the numerical calculation of force-free fields is that of attempting to model the force-free magnetic field of a solar active region, in which case one attempts to find a field pattern that matches certain observational data. A vector magnetograph is now in operation at Marshall Space Flight Center ( Krall et. al. 1982) that yields the vector magnetic field of an active region at the photosphere. In order to compute the corresponding

force-free magnetic field configuration by using the magneto-frictional method, we need to develop an iteration procedure, such as the following. As the first step, we assume an initial set of boundary values for the Clebsch variables  $\alpha$  and  $\beta$  that generate the correct value of the longitudinal magnetic field, and compute the corresponding force-free magnetic field, then compare the observed transverse component of magnetic field at the photosphere with that which arises in the calculation. Based on that comparison, we modify the boundary conditions for  $\alpha$  and  $\beta$ , and repeat the procedure.

Comparison of the configuration of the computed force-free field based on the observed photospheric magnetic field data with the observed field configuration could give a good test for current theories of solar flares and coronal field structures. As pointed out by Krall et. al. (1982), a constant- $\alpha$ , force-free magnetic field ( $\vec{J} = \alpha \vec{B}$ ), i.e. a linear force-free magnetic field is ruled out by the observations of the photospheric magnetic fields. Therefore the capability of computing non-linear force-free magnetic fields of the numerical method developed in this work will be useful in the study of solar magnetic fields and active phenomena on the sun.



## References :

- Alfvén, H., and Fälthammar, C.-G. 1963, *Cosmical Electrodynamics*, (Oxford: Clarendon Press).
- Aly, J. J. 1984, *Astrophys. J.*, **283**, 349.
- Barnes, C. W., and Sturrock, P. A. 1972, *Astrophys. J.*, **174**, 659.
- Berger, M.A., and Field, G.B. 1984, *J. Fluid Mech.*, **147**, 133.
- Birn, J., and Schindler, K. 1981, *Solar Flare Magnetohydrodynamics* (ed. E.R. Priest. New York: Gordon & Breach), p.337.
- Blandford, R.D. 1976, *Mon. Not. R. Astr. Soc.*, **176**, 465.
- Boyd, T.J.M., and Sanderson, J.J. 1969, *Plasma Dynamics*, (New York: Barnes and Noble).
- Bridle, A.H., and Perley, R.A. 1984, *Ann. Rev. Astron. Astrophys.*, **22**, 319.
- Buckley, R. 1981, *Mon. Not. R. Astr. Soc.*, **196**, 1021.
- Chandrasekar, S. 1961, *Hydrodynamic and Hydromagnetic Stability*, (Oxford: Oxford Univ. Press).
- Chandrasekar, S., and Kendall, P.C. 1957, *Astrophys. J.*, **126**, 457.
- Chodura, R., and Schlüter, A. 1981, *J. Comp. Phys.*, **41**, 68.
- Cornwell, T.J., and Wilkinson, P.N. 1981, *Mon. Not. R. Astr. Soc.*, **196**, 1067.
- Courant, R., and Hilbert, D. 1953, *Method of Mathematical Physics*, Vol. 1 (New York: Interscience), p. 175.
- Cowling, T. G. 1957, *Magnetohydrodynamics* (New York: Interscience).
- Davies, J.G., Anderson, B., and Morison, I. 1980, *Nature*, **288**, 64.
- Jackson, J. D. 1975, *Classical Electrodynamics*, (New York: Wiley).

- Kellermann, K.I. 1974, *Galactic and Extra-Galactic Radio Astronomy*, (ed. Verschuur and Kellermann. New York: Spring-Verlag), p.320.
- Königl, A., and Chouduri, A.R. 1985, *Astrophys. J.*, **289**, 173.
- Krall, K. R., Smith, J. B., Hagyard, J. J., West, E. A. and Cumings, N. P. 1982, *Solar Phys.*, **79**, 59.
- Levine, R. H., 1976, *Solar Phys.*, **46**, 159.
- Lüst, R., and Schlüter, A. 1954, *Z. Astrophys.*, **34**, 263.
- Mitton, S., and Ryle, M. 1969, *Mon. Not. R. Astr. Soc.*, **146**, 221.
- Moffatt, H.K. 1983, *Magnetic Field Generation in Electrically Conducting Fluids*, (Cambridge Univ. Press).
- Nakagawa, Y., Raadu, M.A., Billings, D.E., and McNamara, D. 1971, *Solar Phys.*, **19**, 72.
- Nakagawa, Y., and Raadu, M. A. 1972, *Solar Phys.*, **25**, 127.
- Parker, E. N. 1979, *Cosmical Magnetic Fields* (Oxford: Clarendon Press).
- Priest, E. R. 1981, *Solar Flare Magnetohydrodynamics* (ed. E.R. Priest. New York: Gordon & Breach), p.2.
- Priest, E. R. 1982, *Solar Magnetohydrodynamics* (Dordrecht-Holland: Reidel).
- Pringle, J. E. 1981, *Ann. Rev. Astron. Astrophys.*, **19**, 137.
- Rees, M. J. 1984, *Ann. Rev. Astron. Astrophys.*, **22**, 471.
- Sakurai, K. 1972, *Solar Phys.*, **23**, 142.
- Sakurai, T. 1979, *Pub. Ast. Soc. Japan*, **31**, 209.
- Sakurai, T. 1981, *Solar Phys.*, **69**, 343.
- Stern, D.P. 1966, *Space Science Reviews*, **6**, 147.

Sturrock, P. A. 1980, *Proceedings of the Skylab Workshop on Solar Flares* (Colo. Ass. Univ. Press).

Sturrock, P. A. 1985, *Astrophys. J.*, **293**, 52.

Sturrock, P.A. 1985, private communication.

Sturrock, P. A., and Barnes, C. W. 1972, *Astrophys. J.*, **176**, 31.

Sturrock, P. A., and Woodbury, E. T. 1967, *Plasma Astrophysics* (ed. P. A. Sturrock. New York: Academic Press), p. 155.

Sturrock, P. A., and Yang, W. H. 1985, *presented to annual meeting*, SPD, AAS, Tucson.

Sweet, P. 1958, *IAU. Symp.*, **6**, 123.

Woodbury, E. T. 1973, unpublished report.

Yang, W. H., Sturrock, P. A., and Antiochos, S. K. 1986, *Astrophys. J.* **309**, 383.